# Full-Atom Model of the Agonist LPS-Bound Toll-like Receptor 4 Dimer in a Membrane Environment

Alejandra Matamoros-Recio,[a] Juan Felipe Franco-Gonzalez,[a] Lucia Perez-Regidor,[a] Jean-Marc Billod,[a] Joan Guzman-Caldentey,[a] and Sonsoles Martin-Santamaria*[a]

*In memory of Prof. Kilian Muñiz: excellent person, great heart.*

**Abstract:** The Toll-like receptor 4 (TLR4)/myeloid differentiation factor 2 (MD-2) innate immunity system is a membrane receptor of paramount importance as therapeutic target. Its assembly, upon binding of Gram-negative bacteria lipopolysaccharide (LPS), and also dependent on the membrane composition, finally triggers the immune response cascade. We have combined ab-initio calculations, molecular docking, all-atom molecular dynamics simulations, and thermodynamics calculations to provide the most realistic and complete 3D models of the active full TLR4 complex embedded into a realistic membrane to date. Our studies give functional and structural insights into the transmembrane domain behavior in different membrane environments, the ectodomain bouncing movement, and the dimerization patterns of the intracellular Toll/Interleukin-1 receptor domain. Our work provides TLR4 models as reasonable 3D structures for the (TLR4/MD-2/LPS)$_2$ architecture accounting for the active (agonist) state of the TLR4, and pointing to a signal transduction mechanism across cell membrane. These observations unveil relevant molecular aspects involved in the TLR4 innate immune pathways and will promote the discovery of new TLR4 modulators.

## Introduction

Pattern recognition receptors perceive the presence of both pathogen-associated and damage-associated molecular patterns (PAMPs and DAMPs, respectively) and activate the native immune response.[1] Among these receptors, Toll-like receptor 4 (TLR4) is a membrane receptor that specifically recognizes lipopolysaccharides (LPSs) from Gram-negative bacteria through the TLR4 extracellular domain (ectodomain, ED) with the participation of an essential co-receptor, the myeloid differentiation factor 2 (MD-2).[2,3] Thus, the LPS molecule binds to the TLR4/MD-2 system by inserting the fatty acid (FA) chains inside the deep and wide hydrophobic pocket of MD-2, and by establishing a complex network of polar interactions among the LPS oligosaccharide and the TLR4 residues (Figure 1). The agonist conformation of TLR4 is considered to correspond to a (TLR4/MD-2/LPS)$_2$ heterodimer, as observed in the X-ray crystallographic structure of the complex of human TLR4/MD-2 with *Escherichia coli* LPS (LPS$_{Ec}$; Protein Data Bank (PDB) ID: 3FXI).[4] After LPS binding, the dimerization of the TLR4 ED brings together the corresponding cytoplasmic Toll/interleukin-1 receptor (TIR) domains (intracellular domain, ID) which also dimerize. The intracellular ID-ID* dimer recruits the binding of membrane-associated bridging adaptor proteins, such as MyD88-adapter-like (MAL) and TIR-domain-containing adapter-inducing interferon-β (TRIF)-related adaptor molecule (TRAM), triggering the activation of downstream signaling and the inflammatory response.[5,6]

TLR4 has only recently attracted great attention as therapeutic target, and the obtaining of both, agonist and antagonist drugs, is considered a promising strategy for the treatment of a wide range of pathologies, including sepsis, infectious and noninfectious inflammation, central nervous system-related processes, certain autoimmune diseases, allergies, as well as neurodegenerative and tumoral diseases, among others.[7–9] TLR4 agonists can be useful as adjuvants in vaccines and in cancer immunotherapy,[10,11] as exemplified with synthetic nontoxic LPS lipid analogues, as monophosphoryl lipid A derivatives, which are components of vaccines for hepatitis B (Fendrix™), and cervical cancer (Cervarix™).[12] On the other hand, the design and development of LPS mimetics as TLR4 antagonists are being intensively explored for the treatment of inflammation and sepsis, with Eritoran as the main exponent as potent TLR4-antagonist.[9] Although it failed Phase III,[13] Eritoran is under studies for other therapeutic applications.[12] Other examples of TLR4 antagonists include glycolipids, non-LPS like small molecules, and peptidomimetics.[11,12] The possibilities of exploiting TLR4 as a therapeutic target are therefore enormous, with still much to know and learn. In this active research field,

[a] A. Matamoros-Recio, Dr. J. F. Franco-Gonzalez, Dr. L. Perez-Regidor, Dr. J.-M. Billod, Dr. J. Guzman-Caldentey, Dr. S. Martin-Santamaria
Department of Structural and Chemical Biology
Centre for Biological Research Margarita Salas, CIB-CSIC
C/ Ramiro de Maeztu, 9, 28040 Madrid (Spain)
E-mail: smsantamaria@cib.csic.es

Supporting information for this article is available on the WWW under https://doi.org/10.1002/chem.202102995

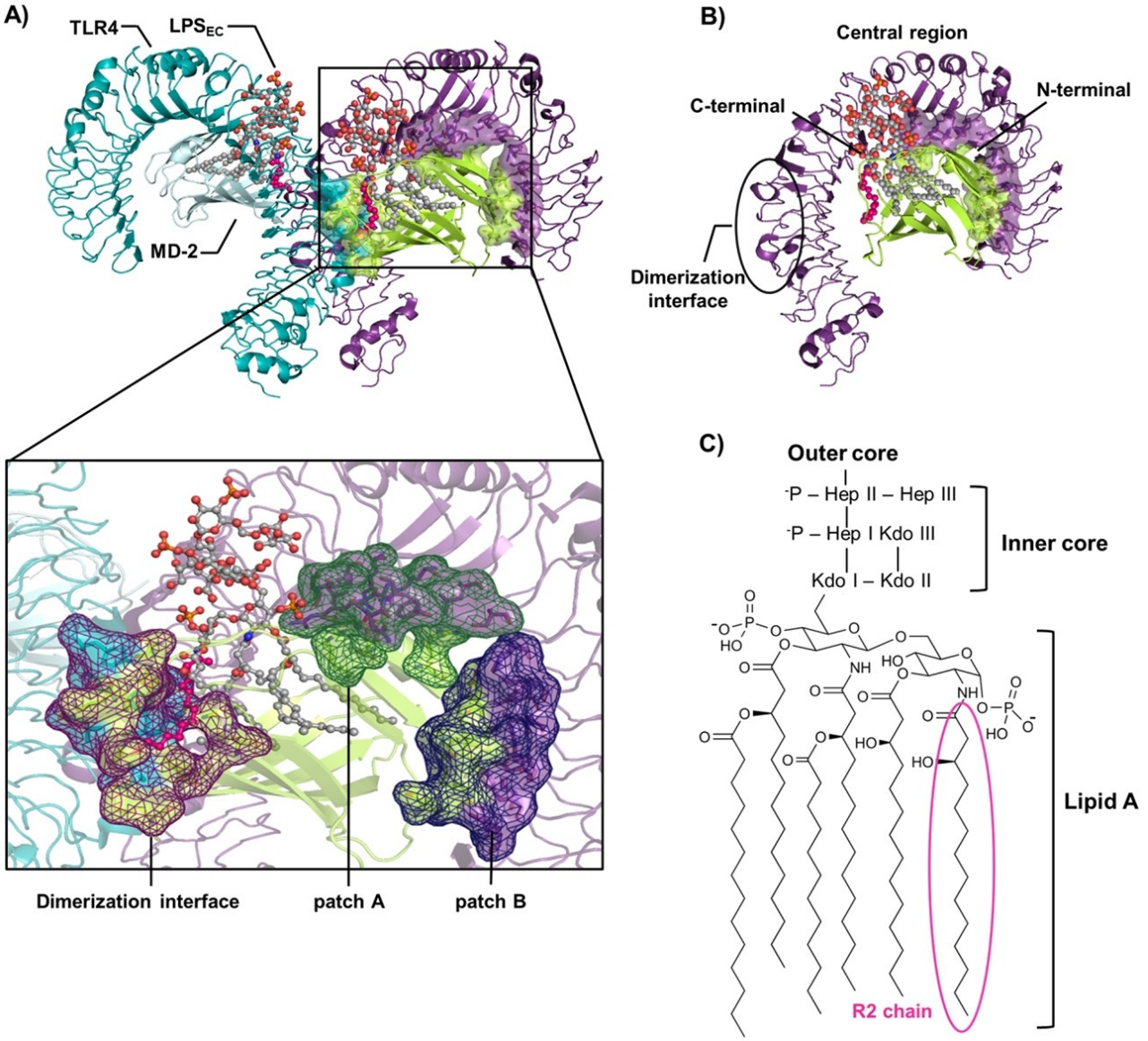


**Figure 1.** 3D structures of the TLR4 ED domain in complex with agonist LPS$_{Ec}$. TLR4 belongs to the superfamily of the leucine-rich repeat (LRR) modules proteins, which have a typical horse-shoe-like conformation. The LRR modules have approximately 20–30 amino acid residues with conserved "LxxLxLxxN" motifs. The whole sequence can be divided in three regions: the N-terminal domain containing modules 1 to 6, a central domain with modules 7 to 12, and the C-terminal domain containing modules 13 to 22. A) Top: Dimeric (TLR4/MD-2/LPS$_{Ec}$)$_2$ X-ray crystallographic structure (PDB ID: 3FXI). Bottom: Primary dimerization interface between the TLR4 chains (TLR4/TLR4*) and contact regions between each TLR4 chain and the corresponding MD-2 (TLR4/MD-2 and TLR4*/MD-2*), which are patches A and B. Patch A corresponds to the N-terminal domain of TLR4 (residues Met1 to Ala251) and patch B to the central domain (residues Gly252 to Lys349). On one hand, the A patch in TLR4 is characterized by being highly evolutionarily conserved, and negatively charged, which allows the interaction with the positively charged MD-2 Arg68 and Lys109 residues of MD-2. On the other hand, the B patch is built by a poorly conserved area, positively charged, and interacts with the negatively charged residues in the F β-strand of MD-2. The parts of MD-2 interacting with the A and B patches of TLR4 are named the A′ and B′ patches, respectively. B) Monomeric TLR4/MD-2/LPS$_{Ec}$ that corresponds to TLR4 and MD-2 chains B, bound to LPS$_{Ec}$, of the TLR4 dimer crystal. TLR4 ED domains, and the TLR4-TLR4* dimerization interface are marked. Protein structures are represented in cyan (TLR4), purple (TLR4*, and TLR4 monomer), pale blue (MD-2) and lime (MD-2*, and MD-2 monomer) cartoon, and LPS$_{Ec}$ as gray CPK. C) Chemical structure of *E. coli* LPS. The R2 fatty acid chain (magenta) placed at the channel of MD-2 completes the dimerization interface.

computational techniques have proven to be efficient approaches to identify molecules with potential therapeutic benefits in TLR4 modulation.[14,15]

It is clear that further insight into the activation mechanism and into the dynamic behavior, both at the atomic-molecular level, can pave new roads for the design and discovery of effective TLR4 modulators. However, most of the molecular basis at atomic level of the TLR4 dimerization and adaptors recruitment processes is still elusive. A relevant aspect to also take into consideration is the membrane environment. The presence of unsaturated fatty acids on the membranes lipids is correlated with liquid-disordered (Ld) phases whereas the presence of saturated fatty acids and cholesterol is associated with liquid-ordered (Lo) phases.[16] In cell membranes, Lo is

known as lipid rafts and play a crucial role during protein signaling.[17] Reported experimental data demonstrate that TLR4 assembly occurs in the plasma membrane rafts, and it is stimulated by LPSs, pointing to a key role of the lipid rafts during the receptor activation process.[18] Deep structural understanding of the molecular recognition events that take place to assemble the TLR4 signaling complex would allow to progress in the understanding of the activation mechanism of this receptor, and in the discovery of novel small molecules with desirable therapeutic properties.

Studies to gain structural and dynamics information about these recognition events required for the TLR4 (activation) dimerization process are scarce due to the high complexity of the receptor. X-ray crystallography, combined with molecular modeling, has provided the atomic details for LPS-ED binding,[4,19,20] while NMR studies have showed that the transmembrane domain (TD) adopts an α-helix structure in bicelles.[21] Combination of multiscale modeling and experimental studies has deepened in the knowledge of the thermodynamics of LPS recognition by the TLR4 ED and TLR4 assembly.[22,23] The monomeric full-length TLR4 structure of different species, including the human, has been predicted by artificial intelligence,[24] and two full-length structural models of human and murine $(TLR4/MD\text{-}2/LPS_{Ec})_2$ heterodimers have also been reported by molecular dynamics (MD) simulation, providing the first notable approaches to the architecture of this important receptor in the agonist-induced state.[25,26] Nevertheless, in these heterodimer models, a simplistic lipid bilayer without cholesterol was used and, in the case of the human TLR4 complex, since a united-atom force field was applied, the hydrogen bonding is not fully taken into account in the TLR4 complex assembly. Additionally, in both full-length models, a limited number of possible transmembrane and intracellular conformations were explored. In any case, providing detailed structural and dynamical information on a heterogeneous and complex system such as a cell membrane is challenging. Current computational simulations have proved proficiency of performing realistic membrane simulations, yielding an invaluable tool to characterize membrane-inserted systems at atomic resolution.[27,28]

We studied each of the TLR4 subdomains-ED, TD, and ID-independently, aiming to propose full TLR4/MD-2 models to rationalize functional and structural aspects involved in the TLR4 activation mechanism. We here report molecular dynamics (MD) simulations of the ED in its dimeric and monomeric forms, in complex with MD-2 engaged by *E. coli* LPS. The TD was simulated in Lo and Ld membrane phases, showing key aspects of the lipid-raft-embedded secondary structure in order to propose several models for TD-TD* dimers. Two probable models for the ID-ID* dimer (symmetric and asymmetric) have also been addressed and their interaction with the bridging adaptor MAL protein has been explored. Four full receptor $(TLR4/MD\text{-}2/LPS_{Ec})_2$ dimers were built and simulated into realistic Lo membrane models, identifying two of them as plausible 3D structures of the full agonist LPS-bound TLR4. We here put together a great effort to bring into agreement the reported experimental data with the insights from the computational perspective. We finally propose full atomistic models of $(TLR4/MD\text{-}2/LPS_{Ec})_2$ dimer that account for conformational, assembly, lipid-raft dependent conformation and thermodynamic properties, revealing pertinent details of the agonist LPS-bound Toll-like 4 receptor and thus, increasing the current knowledge of the lipid rafts role in the TLR4 innate immune signaling pathway.

## Results and Discussion

### TLR4 ED: Dynamic behavior in water

Several X-ray crystallographic structures of the TLR4 ectodomain have been reported and, among them, the structure of the $(TLR4/MD\text{-}2)_2$ heterodimer in complex with $LPS_{Ec}$, the most potent agonist known to date (PDB ID: 3FXI),[4] revealed the interactions at atomic level and the conformational requirements to adopt the heterodimer assembly in the agonist conformation, that is, the necessary structural arrangement to activate the immune response (Figure 1). Also, MD simulations of the TLR4/MD-2 complex engaged by ligands of different kind comprising naturally occurring modulators (e.g., LPS from *Burkholderia cenocepacia*),[29] LPS-like molecules (e.g., fluorescent probes),[30] and non-LPS-like small molecules (e.g., amphiphilic guanidinocalixarenes)[31] have been reported, including the impact of a single point mutation on the receptor activity.[32]

In this work, we performed 100-ns MD simulations of the $TLR4/MD\text{-}2/LPS_{Ec}$ monomer and the $(TLR4/MD\text{-}2/LPS_{Ec})_2$ dimer of the human TLR4 ED in water solution, starting from the X-ray structure (Figure 2). Our simulations show that the interactions at the different interfaces, TLR4/TLR4* (Figure 2A), and TLR4/MD-2* and TLR4*/MD-2 (Figure 2B), were maintained along the simulation in agreement with the reported structural and computational data for the $(TLR4/MD\text{-}2/LPS_{Ec})_2$ complex (Figure S1 and Table S1 in the Supporting Information).[4,33] In contrast, the TLR4 ED monomer exhibits some conformational modifications where the MD-2 chain is separated from the TLR4 ED by a distance of around 4 Å (Figure 3A, green line), and the TLR4 tail is displaced by 18° from the starting geometry (Figure 3B). These results suggest a mutual stabilizing role between both $TLR4/MD\text{-}2/LPS_{Ec}$ units, due to the protein–protein interactions (PPIs) at the dimerization interface upon $LPS_{Ec}$ binding, and reinforce the stabilizing role of MD-2 for TLR4 complexation.[4] Additionally, although *E. coli* LPS exhibits small conformational changes, critical interactions (as shown in the X-ray crystallographic PDB ID: 3FXI[4] structure, and by mutagenesis studies[34]) of this molecule with the corresponding partner TLR4 Phe440 in the dimer, and with MD-2 Phe126 in both, dimer and monomer, were maintained (for details of the $(TLR4/MD\text{-}2/LPS_{Ec})_2$ interactions, see Annex 1 in the Supporting Information). Importantly, the on/off switch Phe126 loop of MD-2 (residues 123–129)[4] did not undergo conformational changes, and the Phe126 remained in an agonist-like conformation in both simulations (Figures 4 and S2). Our unbiased simulations thus provided a reliable optimized ectodomain

 

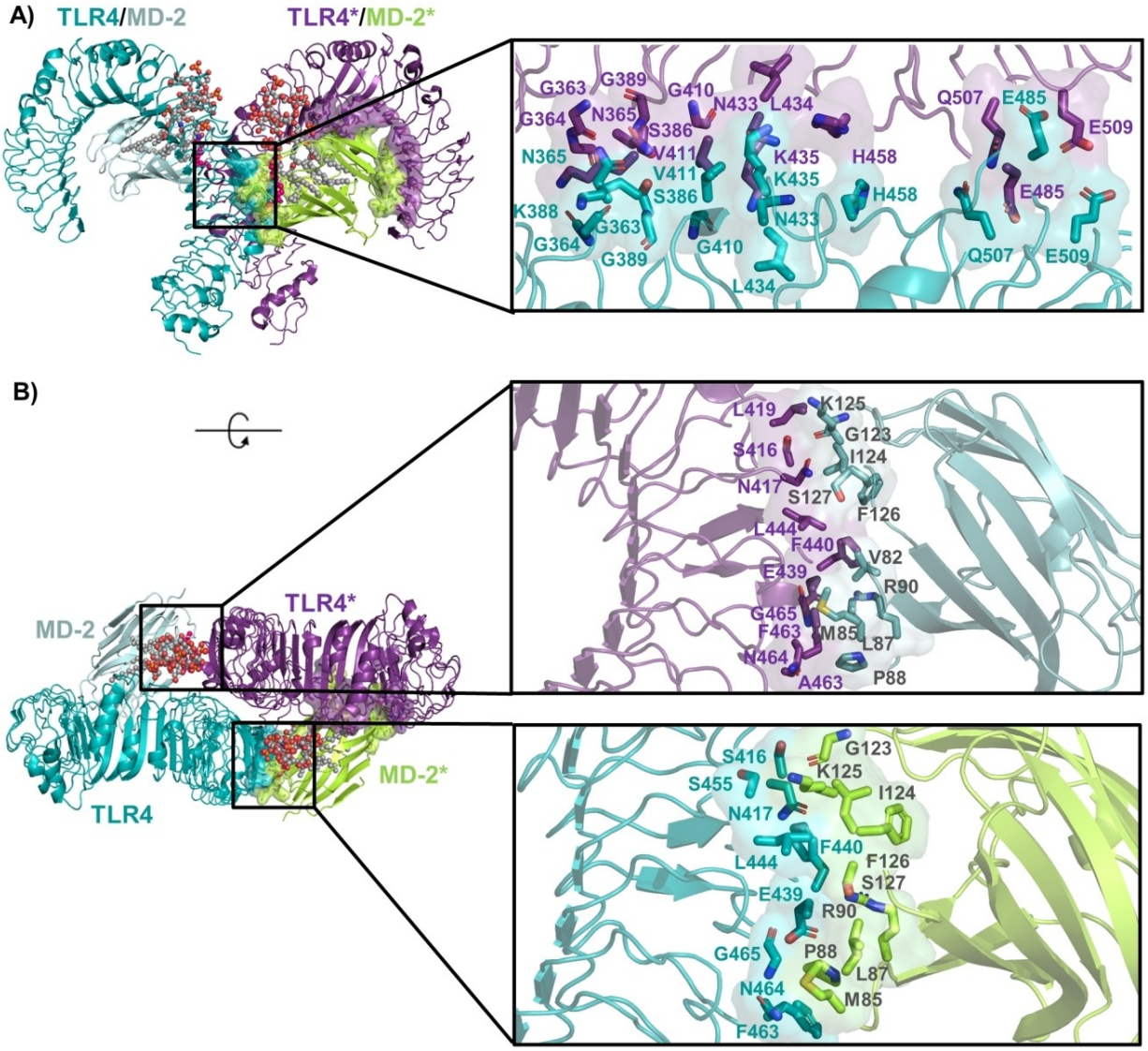


**Figure 2.** Protein-protein interactions present in the dimerized $(TLR4/MD\text{-}2/LPS_{Ec})_2$ average structure from the MD simulations. Left: front and top views of the complex; right: primary dimerization interfaces between TLR4 and TLR4* (A) and between each TLR4 chain and the counterpart MD-2 (B). A) TLR4/TLR4* interface: the interactions include residues located at the central region of the two TLR4 extracellular C-terminal domains (Asn365, Ser386, Val411, Asn433 and Gln507) and other residues from both TLR4 chains (Gly363, Gly364, Lys388, Gly410, Leu434, Lys435, His458, Glu485, Glu509, and Asn531). B) TLR4/MD-2* (and TLR4*/MD-2) interfaces: the interactions involve TLR4 (TLR4*) residues Ser416, Asn417, Glu439, Phe440, Leu444, and Phe463, and MD-2 (MD-2*) residues Met85, Leu87, Gly123, Ile124, Lys125, and Phe126. Contact residues are depicted as sticks with the corresponding labels. Protein structures are represented in cyan (TLR4), purple (TLR4*), pale blue (MD-2) and lime (MD-2*) cartoon, and $LPS_{Ec}$ as gray CPK, with the R2 fatty acid chain colored in magenta.

$(TLR4/MD\text{-}2/LPS_{Ec})_2$ model in agreement with data reported previously by X-ray and computational studies,[4,20,33] and ready to be used in the construction of the full TLR4 system.

### TLR4 TD: Hydrophobic region conformation and membrane composition effect

According to UniProt,[35] the TLR4 TD is predicted to span from Thr632 to Tyr652, and to consist of an α-helix of lipophilic residues with few polar residues. In addition, the amino acid sequence directly following this domain, called hydrophobic region (HR, from Lys653 to Gly670, Figure 5), has been largely argued to actively interact with the membrane, either extending the TD α-helix or interacting with the head groups of the lipids.[36–38] At present, little is known about the conformational changes that occur in the transmembrane α-helices to promote ID dimerization. Mineev et al.[21] reported a combined protein-protein docking and NMR study of both TD and HR of TLR4, pointing to a helical conformation for the HR (from Lys653 to Ala662) in 1,2-dimyristoyl-*sn*-glycero-3-phosphoglycerol (DMPG)/1,2-diheptanoyl-*sn*-glycero-3-phosphocholine (DHPC) bicelles (PDB ID: 5NAM).[21] However, importantly for membrane proteins, both secondary structure and PPIs are known to be lipid membrane composition-dependent.[39] The work of Ruysschaert et al.[38] suggests that the HR domain contains a number

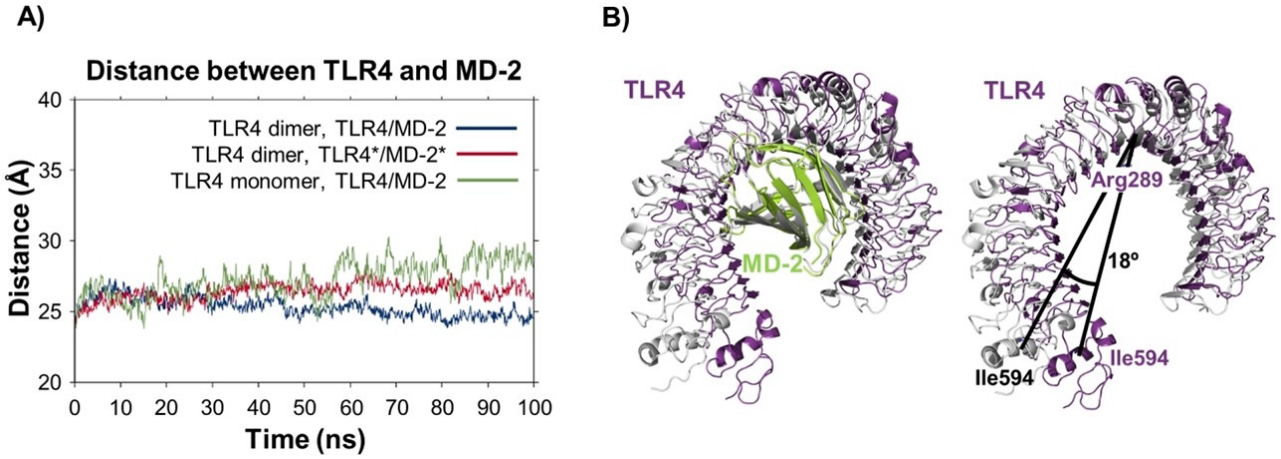


**Figure 3.** Evolution of the TLR4/MD-2/$LPS_{Ec}$ monomer complex over the MD simulation. A) Distance between TLR4 and MD-2 centers of mass, plotted along MD simulations, giving information of how TLR4 chains deviate from their initial position in relation to MD-2. B) Initial structure ($t = 0$ ns) from PDB ID: 3FXI, in gray cartoon, and final conformation ($t = 100$ ns) of the TLR4/MD-2/$LPS_{Ec}$ monomer, in purple cartoon, are superimposed and showing the angle between two arbitrarily selected vectors starting both from the α-carbon (CA) of residue TLR4 Arg289 to, respectively, the initial ($t = 0$ ns) and final ($t = 100$ ns) positions of the TLR4 Ile594 α-carbon (CA). MD-2 is hidden for the shake of clarity.

of potential cholesterol-binding motifs utilized to promote structural rearrangements upon ligand recognition and recruitment into lipid rafts. Then, the HR would adopt an α-helix secondary structure and, thus, would extend the existing transmembrane helix, favoring the ID-ID* dimerization.[38]

To better represent the recruitment of the TLR4 into lipid rafts, we decided to study the dynamic behavior of the TD and HR regions (TD-HR) inserted into two models of symmetric bilayers (Figure 5), namely a Lo membrane (1,2-dipalmitoyl-*sn*-glycero-3-phosphocholine (DPPC)/cholesterol, 60:40), representing the membrane rafts, and a Ld model (1,2-dioleoyl-*sn*-glycero-3-phosphocholine (DOPC)). First, the membrane models were simulated and the results showed to be in agreement with reported data[40] (Figure S3). We then performed 190 ns MD simulations of the TD and the HR both structured as a long α-helix embedded into Ld and Lo membrane models, as reported in the NMR study (PDB ID: 5NAM)[21]. In the Ld bilayer, the transmembrane region entered the membrane, while the HR was exposed to the solvent, without penetrating inside the membrane (Figures 5A, and S4). Interestingly, Lys653 residue, at the TD-HR frontier, is placed close to the phosphate groups of the lower leaflet (cytoplasmic side) of the bilayer and establishes ionic interactions with the anionic head groups. The Lo model exhibits a larger bilayer thickness, compared to the Ld (Figure S3). This allows the TD and part of the HR (from Lys653 to Phe656) to be accommodated inside the membrane (Figures 5A and S4A). As a response to the hydrophobic mismatch, due to the longer TD length in comparison to the bilayer thickness, the TD adopted a slightly titled orientation in the Ld bilayer, with the Lys653 side chain interacting with the phosphate groups, inducing a kink in the helix (Figures 5A and S4B and C). On the contrary, in the Lo membrane, the helix remained perpendicular to the membrane surface, with no signs of tilt or kink angles formation (Figures 5A and S4B–D). In both cases, Lo and Ld, the TD and part of the HR (from Lys653 to Ala662), maintained the α-helix secondary structure (Figure S4E and F).

We also performed MD simulations starting from the TD α-helix attached to the HR peptide with an extended unstructured conformation (Figures 5B and S5). The resulting TD-HR was embedded into Lo and Ld membranes and, after 250 ns of simulation, the HR was observed to adopt an α-helix secondary structure in both membrane models (Figures 5B and S5). This result disagrees with the hypothesis proposed by Ruysschaert et al.[38] which indicated that HR would adopt the α-helix secondary structure only when inserted in a cholesterol-containing membrane. The kink region (Lys653-His657) remained as an unstructured conformation in both bilayer models (DSSP[41] analysis in Figure S5), also in accordance with the reported NMR data.[21]

Going further into the folding properties of the HR segment, we performed a MD simulation in water starting from an extended conformation. Along the MD simulation, the peptide adopts an α-helix structure (Figure S6) in agreement with the HR region when it is outside the membrane, exposed to the aqueous medium. As a matter of fact, this secondary structure corresponds to the one elucidated by NMR,[21] and is associated to the insertion in the membrane. The presence of hydrophobic residues appears to be critical for the helix formation in the polar medium. Hence, we cannot discard that this HR segment can be exposed to the aqueous environment outside the membrane.

Our results point to a short portion (Lys653-His657) inside the TD-HR sequence that could not correspond to a structured α-helix under certain conditions of the surrounding medium. Therefore, while a continuous helix for the transmembrane plus the hydrophobic region is possible, our simulations suggest the Lys653 kink regulates the final placement of the HR, depending on the membrane composition, that is, as a prolonged helix in the Lo membrane or as a bent helix in the Ld membrane. This

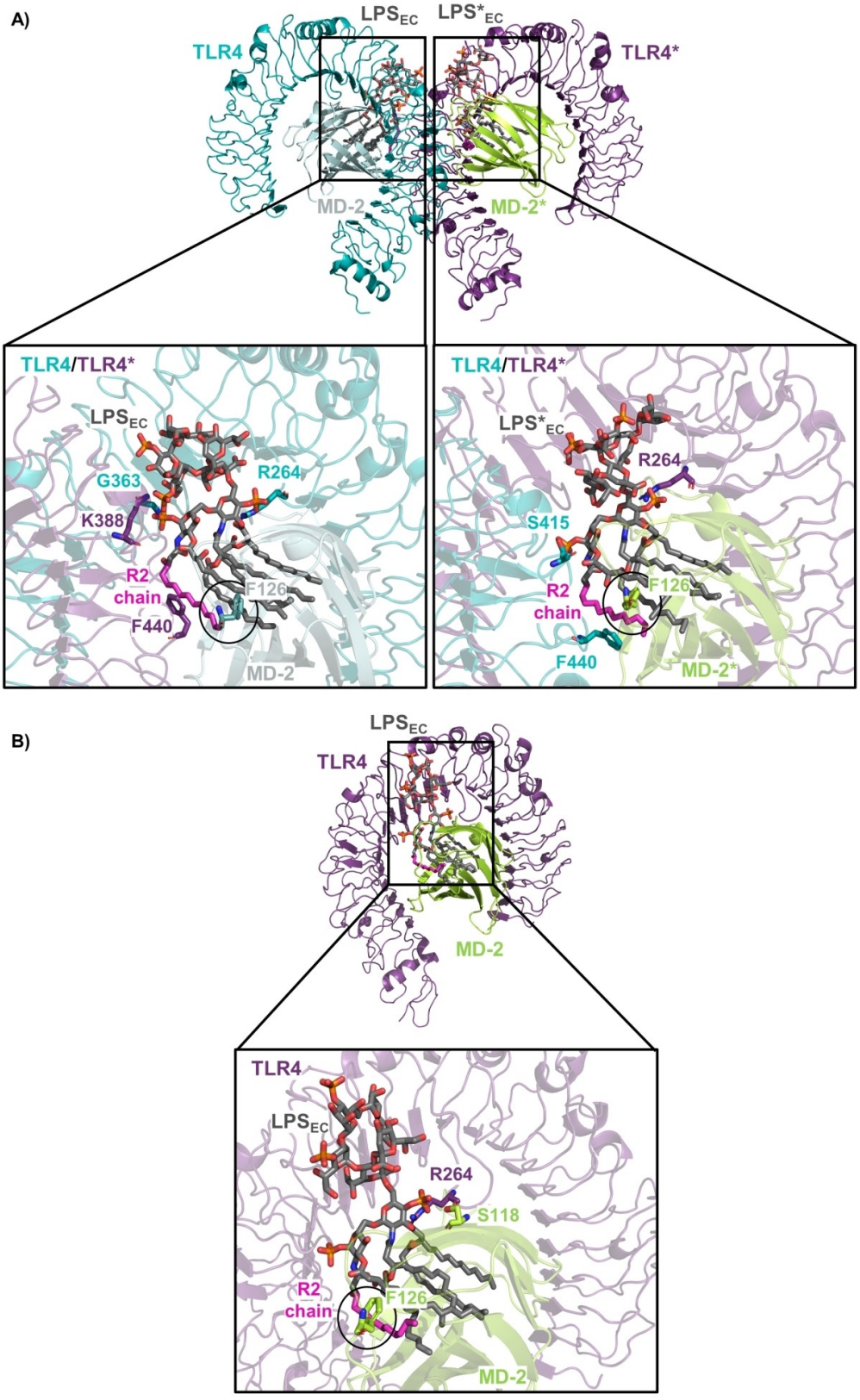


**Figure 4.** Binding mode of $LPS_{Ec}$ to TLR4. Details of the interaction in the A) $(TLR4/MD\text{-}2/LPS_{Ec})_2$ dimer and B) $TLR4/MD\text{-}2/LPS_{Ec}$ monomer average structures from the MD simulations. As observed, MD-2 Phe126 is in the agonist conformation, pointing towards the MD-2 cavity. Contact residues are depicted as sticks with the corresponding labels. Protein structures are represented in cyan (TLR4), purple (TLR4*), pale blue (MD-2) and lime (MD-2*) cartoon, and $LPS_{Ec}$ as gray sticks, with the R2 chain colored in magenta.

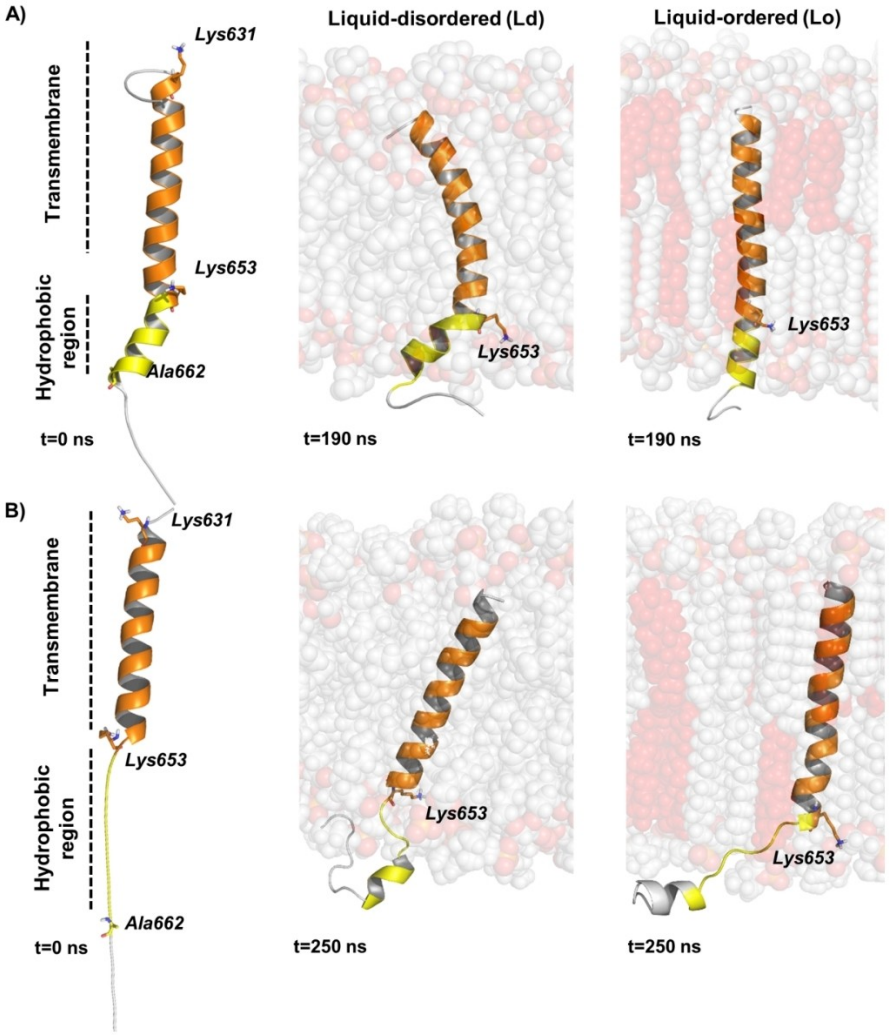


**Figure 5.** MD simulations of TLR4 TD (orange) and HR (yellow) in Ld (left) and Lo (right) membrane models. A) The TD plus HR α-helix structure was retrieved from PDB ID 5NAM. B) The TD was built as an α-helix and HR, built in an extended-coil conformation, was attached to it. At the end of the simulation, the HR is folded underneath the membrane in both membrane models. Lys631, Lys653 and Ala662 are represented as sticks; the TD and the HR are represented as orange and yellow cartoon, respectively. The membrane is in gray spheres, with cholesterol colored in red, and the solvent and ions are hidden.

finding provides a precise molecular perspective to the proposed mechanism for clustering partner TLR4 monomers: only the Lo membrane would be able to embed the full TD–HR α-helix, thus rigidifying the Lys653-kink, stabilizing the intracellular domain, and allowing the ID-ID* recognition and dimerization. Accordingly, the Lo membrane model was selected for the following studies.

### Does TD-TD* dimerization occur by a preferred face/side?

In order to propose plausible TD-TD* dimer models, two different approaches were used by means of TMDOCK[42] and PREDDIMER[43] algorithms. Each program generated six possible TLR4 TD-TD* symmetric α-helical dimers, comprising residues from Lys631 to Ala662, with alternative dimerization interfaces (Figure S7). Based on the geometry, a right-handed crossed disposition between the TD-TD* dimers seems to be predominant,[44] with varying crossing angle (Tables S2 and S3). Only one model predicts a parallel disposition. The dimer contact area was shifted towards the N-terminus in six of the total models, in agreement with NMR reported data,[21] whereas the remaining five dimers crossed by establishing contacts at the center of the TD residues (Figure S7). All predicted TD-TD* models were geometrically compatible with a merged ectodomain dimer (from PDB ID: 3FXI)[4] and plausible ID-ID* models (see below).

The predicted TD-TD* models went through a restrained minimization and scoring procedure (see Experimental Section). The local scores assigned to the models ranged from 0.60 to 1 (in the top 40% best range), and the global scores ranged from 0.52 to 0.58, suggesting sufficient structural quality (Table S4).[45] The only exception was the parallel packed model (model 6, obtained from PREDDIMER approach), with lower local scores, ranging from 0.34 to 0.87. Clustering of the predicted models, in terms of helix-helix dimerization interface (see Experimental

Section), revealed two main dimerization interfaces (interfaces I and II, Figure S8) with similar scores (Table S4). The dimerization interface I, from cluster 1, includes residues Ile634, Ser637, Val638, Val641, Ser645, Ala648, Tyr652 and Phe656, whereas dimerization interface II, from cluster 2, contains residues Ile633, Ser637, Val641, Val644, Ala648, Val651, Tyr652, Tyr655 and Phe656 (Figure S8B). Models from each cluster showed common residues at the dimerization interface, but different crossing angles. Interestingly, residues Val636, Leu639, Leu642, Val646, Val647 and Leu660, which have been predicted to form part of the TD dimerization interface by NMR studies,[28] were exposed to the hydrophobic core of the bilayer in all the models, in agreement with the docking-based TD-TD* models predicted by Patra et al.[25] (Figure S8C). According to these authors, this observation suggests the existence of alternative dimerization interfaces or the possibility of oligomerization. However, although isolated TDs of TLRs form oligomers in solution,[46] TLR4 does not oligomerize in vivo.[47] Thus, the predicted TD dimers could represent distinct active states of the TLR4 TD in different environments, and/or TLR4 cellular localizations, rather than different oligomerization interfaces.[21,44]

Building our way up to the TLR4 full-length complex model, we selected the TD-TD* model with the best ranked score[45] from each cluster (hereinafter referred to as TD1 from cluster 1, and TD2 from cluster 2) as potential TD dimers for further study (Figure 6, and details at Annex 2 in the Supporting Information). Thus, MD simulations of these two models (TD1 and TD2) were performed in a Lo model of the membrane (Figure S9A). From the TD-TD* contact maps after the simulations (Figures S9B), it can be observed that TD2 model exhibits TD-TD* contacts all along the TD domain, including helix and HR region, while TD1 model shows most of TD-TD* contacts at the top of the helixes. The two models reached stabilized conformations with crossing angles between the helical axes of $-36^\circ$ and $-20^\circ$ for the TD1 and TD2, respectively (Figure S9C). These observations can indicate that dimer packing is more efficient in TD2 model than in TD1 model. The contact maps showed contacts between residues Thr632, Ile633, Val636, Ser637, Ser640, Val641, Val644, Val649, Tyr652, Phe656 and Leu660, pointing to their relevant role as key components of the dimerization interface.[44] In both models, the unfavorable hydrophobic mismatch with the hydrophobic core of the membranes was observed. As a consequence, in the TD2 dimer, the HR induced a kink in one $\alpha$-helix, involving the interaction of Lys635 with the phosphate headgroups of the membrane lipids, whereas in the TD1, the helixes adopted a curved conformation to overcome hydrophobic mismatch by avoiding exposition to solvent (Figures S9A, and S9D and E). Finally, it was observed that the helical structure is lost in the C-terminal region, which might be due to the absence of the ID domain, and to the additional rigidity provided to the TD terminal regions.

### TLR4 ID: Two models of dimerization are possible

Although it has been reported that isolated TLR4 ID domains do not form stable dimers in vitro,[48] experiments using mutants and cell-permeable inhibitory peptides have revealed that different arrangements for the ID-ID* dimer are possible, after the TLR4 activation.[49–52] Also, the lack of structural information for the intracellular TIR domain of TLR4 has promoted the building of computational models,[15] clearly showing the role of the BB loop for the homodimerization, without excluding the participation of other structural elements, as the $\alpha$E helixes (Figure 7A). Therefore, from the structural perspective, two possible dimerization modes would be possible: the "face-to-face", and the "back-to-face".[48] The first model of the TLR4 ID dimer was based on the X-ray crystal structure of the TLR10-ID homodimer,[53] which places the $\alpha$C helix and the BB loop of each subunit in between the dimerization interface, interacting

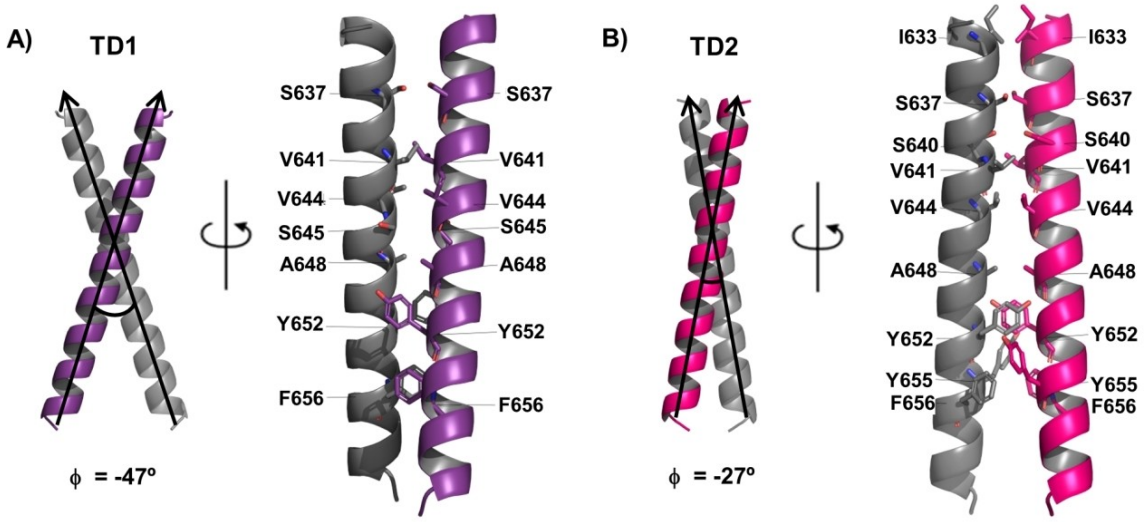


**Figure 6.** TLR4 TD-TD* dimer models. Representation of the crossing angle and details of the contacts present in the selected models, TD1 (in purple and gray) and TD2 (in magenta and gray). TD1 and TD2 models are right-handed crossing dimers, with angles of $-47^\circ$ and $-27^\circ$, respectively. Contact residues are represented as sticks, with the corresponding labels. Protein structures are represented in cartoon form.

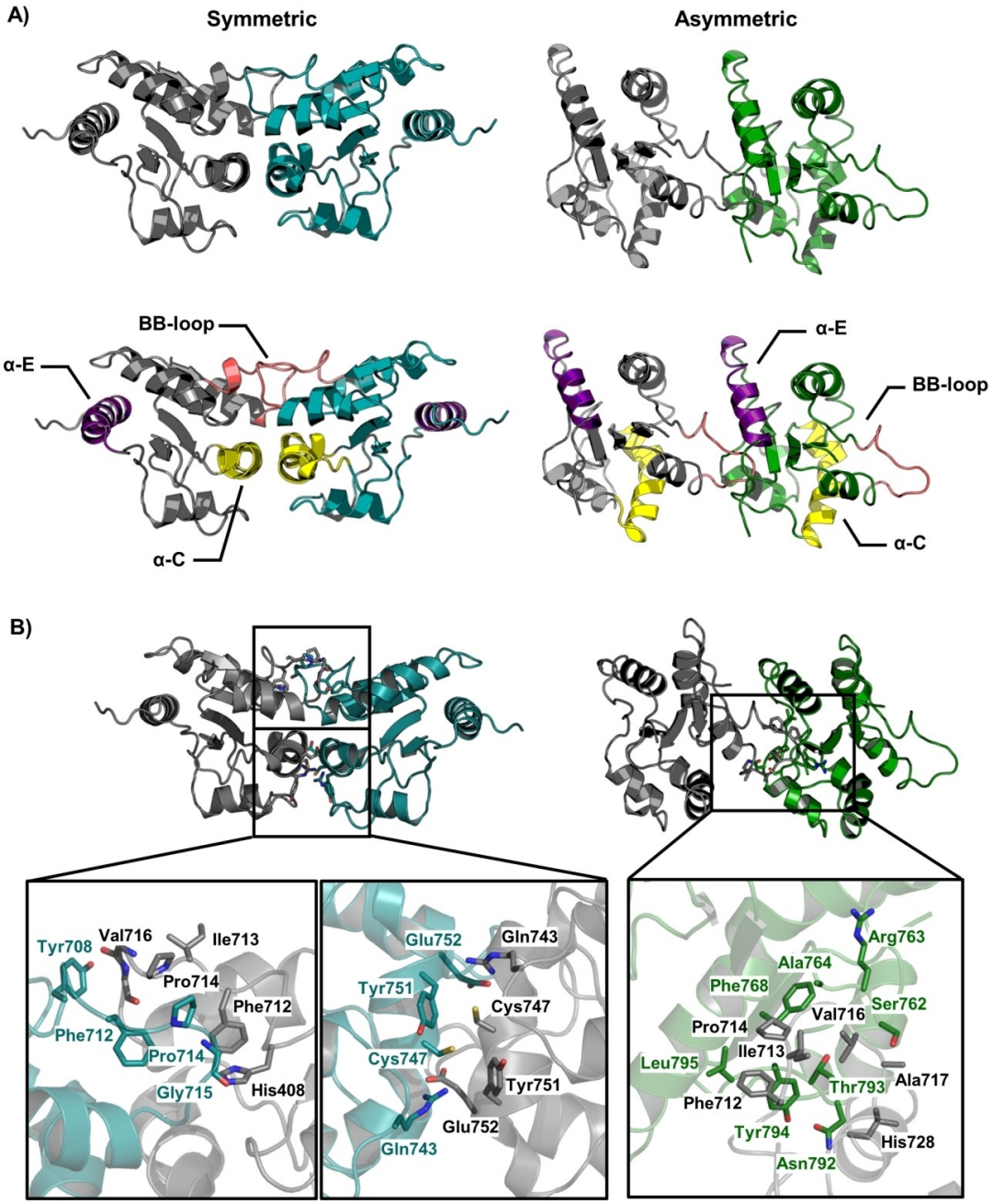


**Figure 7.** Intracellular TIR domain of TLR4 (ID-ID* dimer). A) 3D representation of the symmetric homology model, and the asymmetric protein-protein docking model, with details on its structural composition. BB loops are shown in salmon pink, and α-C and α-E helices in yellow and purple, respectively. B) A close-up of the dimerization interface interactions. TLR4 chain A is in gray and chain B in blue (symmetric model) or green (asymmetric model) cartoon. Residues interacting at the protein-protein interface are represented as sticks with the corresponding labels.

with their counterparts in a "face-to-face" symmetric manner (Figure 7 A).[54] Alternatively, the use of a decoy peptide approach has suggested an alternative "back-to-face" asymmetric dimerization mode in the TLR4 ID, with the αE helix of one monomer and the BB loop of the counterpart forming the interface.[49] A remarkable example of the "back-to-face" interaction in a TIR-domain-containing protein is observed in the MAL cryogenic electron microscopy (cryo-EM) structure, published by Ve et al.,[6] where MAL assembles by forming stable protofilaments in a head-to-tail arrangement (Figure S10). Given the high conservation of the interface residues among proteins containing TIR domains, including TLR4 ID, the authors suggest this arrangement as a reasonable mode to establish PPIs between the intracellular TLR4 TIR domain and the adaptor proteins. This would then result in a head-to-tail asymmetric TLR4 ID-ID* dimer, capable to interact with bridging adaptor proteins, such as MAL or TRAM. Considering these precedents, we decided to construct two possible dimer models for the

dimerization of the ID: the symmetric ("face-to-face") and the asymmetric ("back-to-face") manners (Figure 7 A).

The symmetric ("face-to-face") dimer model was built by homology modeling (see the Experimental Section), retaining 5 templates to base the building process on the TIR domains of human TLR1, TLR2 (P681h mutant), TLR2 (C713s mutant), TLR6 and TLR10. The resulting dimer exhibited great similarity with that published by Núñez-Miguel et al.,[54] and good overlapping of the ID monomer with that predicted by artificial intelligence[24] (RMSD of 1.468 Å). The model presents a dimerization interface formed by residues Cys747, Tyr751, Glu752 and Arg780 from the BB loop, and residues Tyr709, Phe712, Pro714 and Gly715 from the αC helix (Figure 7 B). These residues are reported to be important for TLR4 dimerization and adaptor proteins recruitment, according to mutagenesis studies.[50,51]

The asymmetric ("back-to-face") dimer model was built following the architecture of MAL protein cryo-EM structure (PDB ID: 5UZB).[6] We performed guided protein–protein docking to generate TLR4 ID-ID* with residues in contact from the BB loop and the αE helix, whose mutations have demonstrated to disrupt the ID-ID* dimer formation.[51] Among them, we selected the best predicted pose which showed structural overlapping with the MAL structure (PDB ID: 5UZB,[6] Figures 7 A and S10). The dimerization interface is formed by residues Arg710, Phe712, Ile713, Pro714, Gly715, Val716 and Ala717 from the BB loop, and His728 from the BC loop of one monomer protruding into a groove formed by residues Ser762, Arg763, Ala764 and Phe768 from the CD loop, Asn792, Thr793, Tyr794 and Leu795 from the DE loop and Arg810, Lys813 and Ala814 from the αE helix of the counterpart monomer (Figure 7 B).[8]

Both, the symmetric and asymmetric dimer complexes were submitted to 150 ns MD simulations in water, observing high stability of the PPIs, as well as the 3D conformation (Figure S11 A and B). We characterized the motion of the chains independently in both models and noted higher motion of the CD and DD loops in the symmetric dimer, and of the DD loops and αB and αE helixes in the asymmetric one (Figure S11 C and D). The averaged contact map along the simulation shows interactions between the BB loop and αC helix from both chains in the symmetric model, and between the BB loop from chain A and the CD loop and αE from chain B in the asymmetric model (Figure S11 E), in agreement with the mutagenesis studies that identified residues and regions crucial for the dimerization of the ID and the activation of TLR4.[51] Our molecular docking and MD studies add new evidence that two dimerization patterns are possible for the TLR4 intracellular TIR domain: symmetric and asymmetric, in agreement with reported functional data[50,51] that suggests that TLR4 intracellular signaling may be regulated by different structural elements of TLR4 TIR domain, pointing to the possibility of pathway-specific interaction surfaces.[55]

**Can MAL protein bind to both ID-ID* dimers?**

After obtaining two plausible intracellular dimer models, the following question that immediately arose was whether they could both be able to recruit adaptor proteins. We used the bridging adaptor protein MAL as validation tool, and performed the docking (retrieved from PDB ID: 5UZB)[6] into the two TLR4 intracellular models, symmetric and asymmetric (Figure 8). All the docked poses showed MAL binding to the ID-ID* dimers at the dimerization interface.

In the TLR4 ID-ID* symmetric model, the docking of a MAL monomer showed that two possible TLR4 binding interfaces were possible (Interfaces 1 and 2, Figure 8 A). The interfaces involved residues from the CD and DD loops, and the αC and αD helixes of both TLR4 subunits (Figure S12). These regions are adjacent sites which could build an extended platform for adaptors binding, in agreement with mutagenesis studies about binding interfaces with MAL protein.[51]

To check the stability of the complexes between the symmetric TLR4 ID-ID* with MAL protein, and to gain insights on the interactions that take place, we performed a series of 150 ns MD simulations of several complexes from the best-docked solutions (for further details see Annex 3 in the Supporting Information, and Figures S13–S15). MD simulations of the symmetric TLR4 in complex with MAL reveal that the αE helix of MAL protein is required as a recognition motif, in order to form stable TLR4/MAL complexes. Moreover, MAL could interact with the symmetric TLR4 ID-ID* as a monomeric subunit or as homodimer. It is widely accepted that the TLR4 BB loops are the site of ID dimerization and adaptor recruitment.[56] Nevertheless, in all our symmetric TLR4/MAL models, these loops are found on the opposite face of the TLR4 predicted regions for MAL binding. On this matter, it is important to mention that the reported mutations of the residues from the TLR4 BB loop affect both, the TLR4 ID dimerization and the adaptors recruitment.[51,52] A probable explanation for this observation could be that the mutations which involved residues that are directly implied in the TLR4 ID-ID* dimerization interface, such as those comprising the BB loops, would disrupt the TLR4 dimer and therefore, would indirectly interfere in the interaction between TLR4 and the adaptor proteins.

As for the asymmetric ID-ID* model, we wondered whether MAL could bind following a sequential assembly, as proposed in the cryo-EM MAL architecture,[6] *i.e.*, once the TLR4 ID dimer is performed, one monomer of MAL is recruited, followed by the recruitment of a second MAL subunit (Figure S11). Based on the proposed sequential binding of MAL to TLR4,[6] we performed two independent docking calculations between the TLR4 dimer and the dimer of MAL and one monomeric subunit of MAL (Figure 8 B). The docking calculations were guided following not only mutagenesis studies on the TLR4 TIR intracellular domain, but also on data from MAL protein mutagenesis (see Experimental Section).[50–52] Docking results revealed that the asymmetric ID-ID* model could interact with both, the monomeric and the dimeric forms of MAL protein (Figure 8 B, Annex 3 and S16 A), by reproducing the structural arrangements observed in the cryo-EM MAL assembly (Fig-

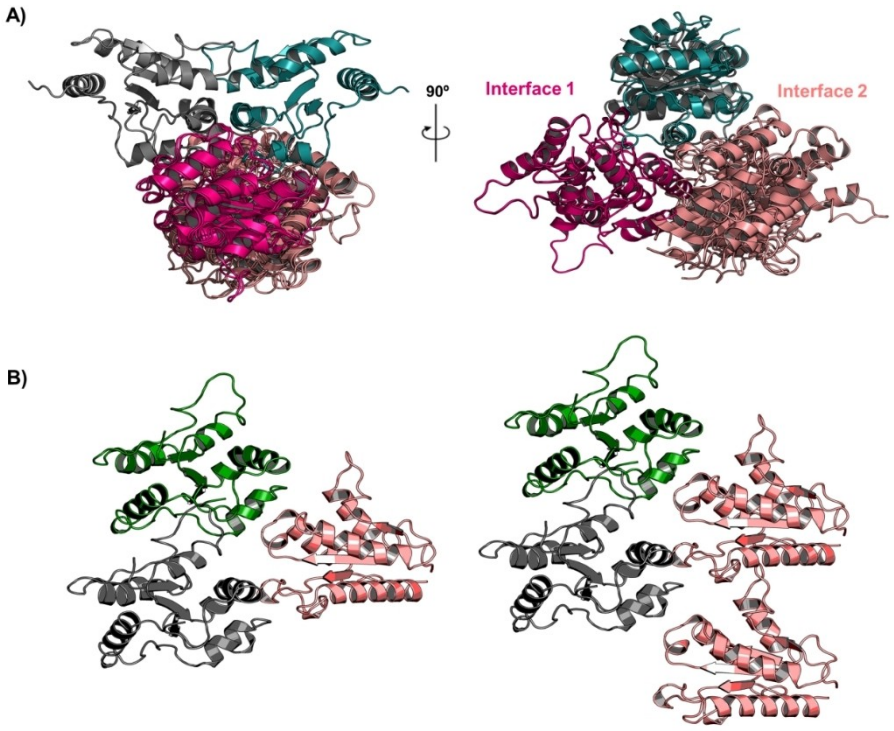


**Figure 8.** Protein–protein docking of the TLR4 TIR domain (ID-ID* dimers) and MAL protein (PDB ID: 5UZB). A) Front (left) and side (right) views of the best-docked poses of a MAL monomer to the TLR4 ID-ID* symmetric model. Docking results revealed that two binding interfaces (Interfaces 1 and 2) are possible. B) Selected docked pose of a MAL monomer (left) and the MAL dimer (right) to the TLR4 ID-ID* asymmetric model. MAL docked poses were selected following the arrangement observed in MAL filament cryo-EM structure (PDB ID: 5UZB), based on the structural similarity between TLR4 and MAL TIR domains. TLR4 chain A is shown in gray and chain B in blue (symmetric model) or green (asymmetric model) cartoons. MAL poses binding at the symmetric TLR4 Interface 1 are in colored in magenta, whereas those interacting at Interface 2, and with the asymmetric TLR4 dimer, are in salmon pink.

ure S11).[6] Subsequent 150 ns MD simulations of selected asymmetric TLR4/MAL docked complexes were performed. The complexes remained stable during the whole simulations, and, the network of PPIs at the MAL binding interface was maintained during the whole simulation (Figure S16 B).

Altogether, our studies of the isolated TLR4 TIR dimers suggest that both symmetric and asymmetric ID-ID* models are suitable for MAL binding, either as a monomer or homodimer, with favorable predicted binding affinities (Annex 3, Tables S6–S8). These results corroborate the two proposed dimerization patterns for the TLR4 intracellular TIR domain as deduced from our docking and MD studies (preceding section).

### Full TLR4 dimer: The TLR4/MD-2 ectodomain bouncing movement

The study of the independent TLR4 domains led us to a better understanding of the dimerization/assembly processes, the key protein-protein interactions implicated in the dimerization, and the role of membrane composition. Nevertheless, these studies provide partial views of a more complex problem, so the model of the full-length TLR4 dimer inserted into the membrane is definitively required to advance into the complete description of the TLR4.

Our computational studies of the individual TLR4 domains provided robust models as starting points to face the assembly of the full-length $(TLR4/MD\text{-}2/LPS_{Ec})_2$ heterodimer in the active conformation and inserted in a Lo membrane model. We constructed two different systems based on the asymmetric and the symmetric ID-ID* dimers, with both types of TD1 and TD2 models (Figure 9) and submitted the resultant four systems to 350 ns MD simulations (Figures 10 and S17). The PPIs described above for the $(TLR4/MD\text{-}2/LPS_{Ec})_2$ complex were kept in all full-length models. These include the interactions exhibited in the dimerization interface and between TLR4 and MD-2, through both patches, A and B (Figure S18). Therefore, as expected, MD-2 Phe126 residue maintained the closed (agonist/active) conformation (Figure S19).

To reveal an energy-structure relationship for our proposed full-length models, the TLR4-TLR4* energy interaction was calculated and correlated with several geometrical parameters. We calculated the Gibbs free energy ($\Delta G$) for TLR4-TLR4* PPIs (between chain A and chain B), the ED-membrane surface interaction defined by angle $\theta$, the arrangement *cis*/*anti*/*gauche* between the extracellular and intracellular domains which is defined by the dihedral angle $\psi$ and the cross angle formed by both transmembrane helixes ($\phi$; angles $\theta$, $\psi$, and $\phi$ are defined in Figure 11 A, below).

Along the MD simulations of the four full-length models, it was observed that the ED tilts towards the membrane in an

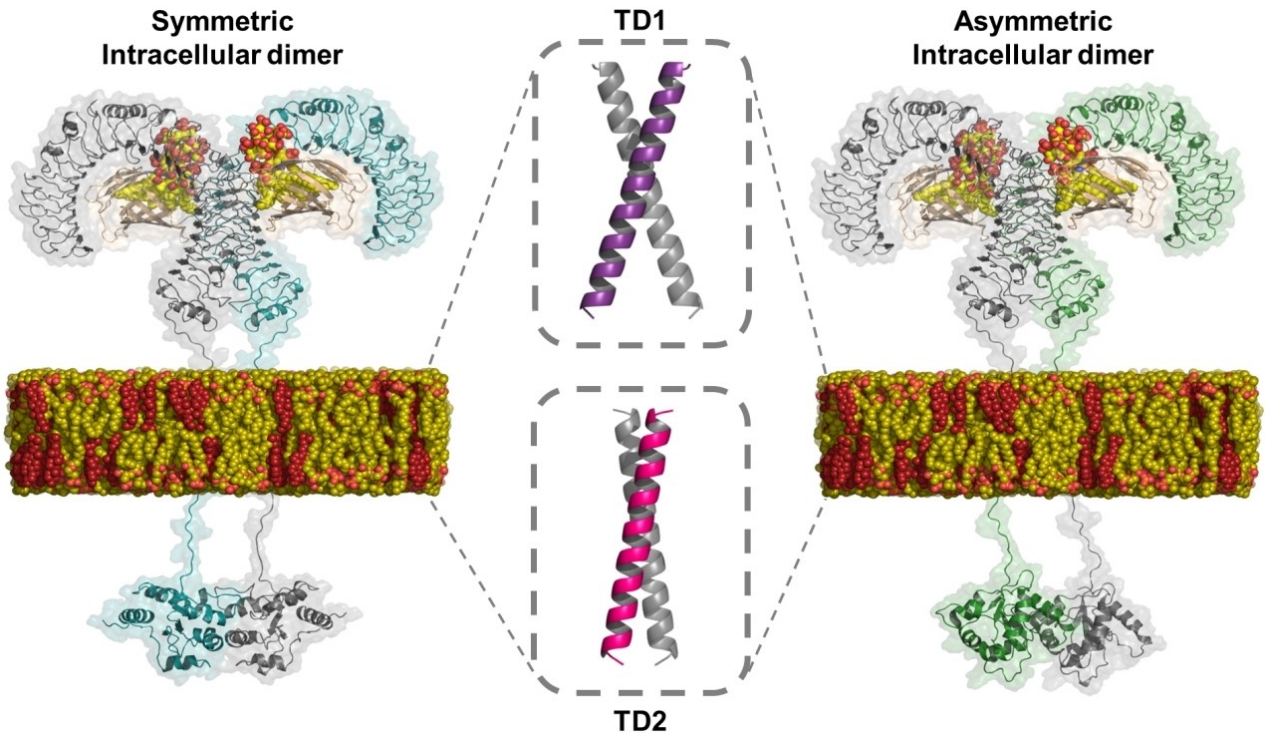


**Figure 9.** Schematic representation of the full-length initial model (TLR4/MD-2/$LPS_{Ec}$)$_2$ building process, embedded in a Lo model membrane. 3D structures correspond to the X-ray crystallographic structure for the ED domain (PDB ID: 3FXI), ab initio modeling for the TD domain (TD1 and TD2), and homology modeling and protein–protein docking for the ID domains (symmetric and asymmetric models). Protein structures are represented in cartoon and semitransparent surface. Full-length TLR4 chain A is in gray, and chain B is in blue or green for the symmetric or asymmetric model, respectively. MD-2 is in salmon pink. The A chain of the TD1 and TD2 models is colored in purple (TD1) or magenta (TD2), and the B chain in dark gray. $LPS_{Ec}$ and membrane lipids are depicted as yellow spheres, with their phosphate groups as red spheres, and membrane cholesterol as garnet spheres. Solvent molecules and counterions are omitted.

alternating fashion (Figure 10), that is, at a given time a TLR4 unit interacts with the membrane surface ($\theta > 30°$, definition of $\theta$ in Figure 11 A) whereas the second TLR4 chain stays away from the membrane surface ($\theta < 30°$). This observation results in a bouncing movement for the ED dimer, during the explored trajectory, along which the TLR4 ED interacts with the membrane outer leaflet (Figure 10, Annex 4, and Figure S20). In the four full-length models, independently of the particular TD-TD* and ID-ID* dimerization patterns, when we observe the bouncing movement at the ED as a function of the Gibbs free energy, the lowest energetic conformations are exhibited when the ED is tilted towards the membrane (Figure 11 B–E, black spots at $\{\theta_A$ or $\theta_B\} < 30°$). This suggests that the TLR4 ED is very dynamic in the membrane environment, and the tilted conformation of the TLR4 stabilizes the TLR4-TLR4* PPI interface.

To our knowledge, this bouncing movement was not observed in previously reported simulations of the full-length TLR4, which did not mimic physiological conditions required for the activation of the receptor (i.e., LPS binding, and receptor recruitment into lipid-rafts). The ED collapsed into the membrane without tilting back up, with non-cholesterol membrane content, and in the absence of TLR4 bound ligand (human TLR4, $t = 100$ ns,[25] and murine TLR4, $t = 2$ μs,[26] respectively). Interestingly, in the case of the murine TLR4,[26] the bouncing was reported when considering a membrane model with glucosylceramide, pointing to the role of the membrane composition in order to study these events.

Bouncing movement of the ED has been reported for other biological systems.[57,58] Indeed, experimental and computational studies demonstrated that transient interactions between the ectodomain and the membrane outer leaflet, regulate the function of transmembrane receptors such as the epidermal growth factor receptor,[57] and the integrin receptor.[58] Moreover, signal transduction across cell membranes can occur within lipid–protein interactions, additionally to direct protein–protein interactions, as seen in GPI-anchored receptors lacking transmembrane domains.[59] In summary, the ED bouncing of the TLR4 might regulate the interaction of the receptor with other related transmembrane proteins, like CD14, which is essential for TLR4 endocytosis,[3] suggesting a key role of such bouncing on the control of receptor signaling across the plasma membrane.

### Full TLR4 dimer: The TD-TD* dimer options

To reveal the correlation between the TD conformation and the ED arrangement, we monitored angle $\phi$ as function of $\psi$ (Figures 11 A and 12 A–D). The so-called symmetric full models exhibited the larger $\phi$ values which range from $\phi \sim 30$–$41.2°$,

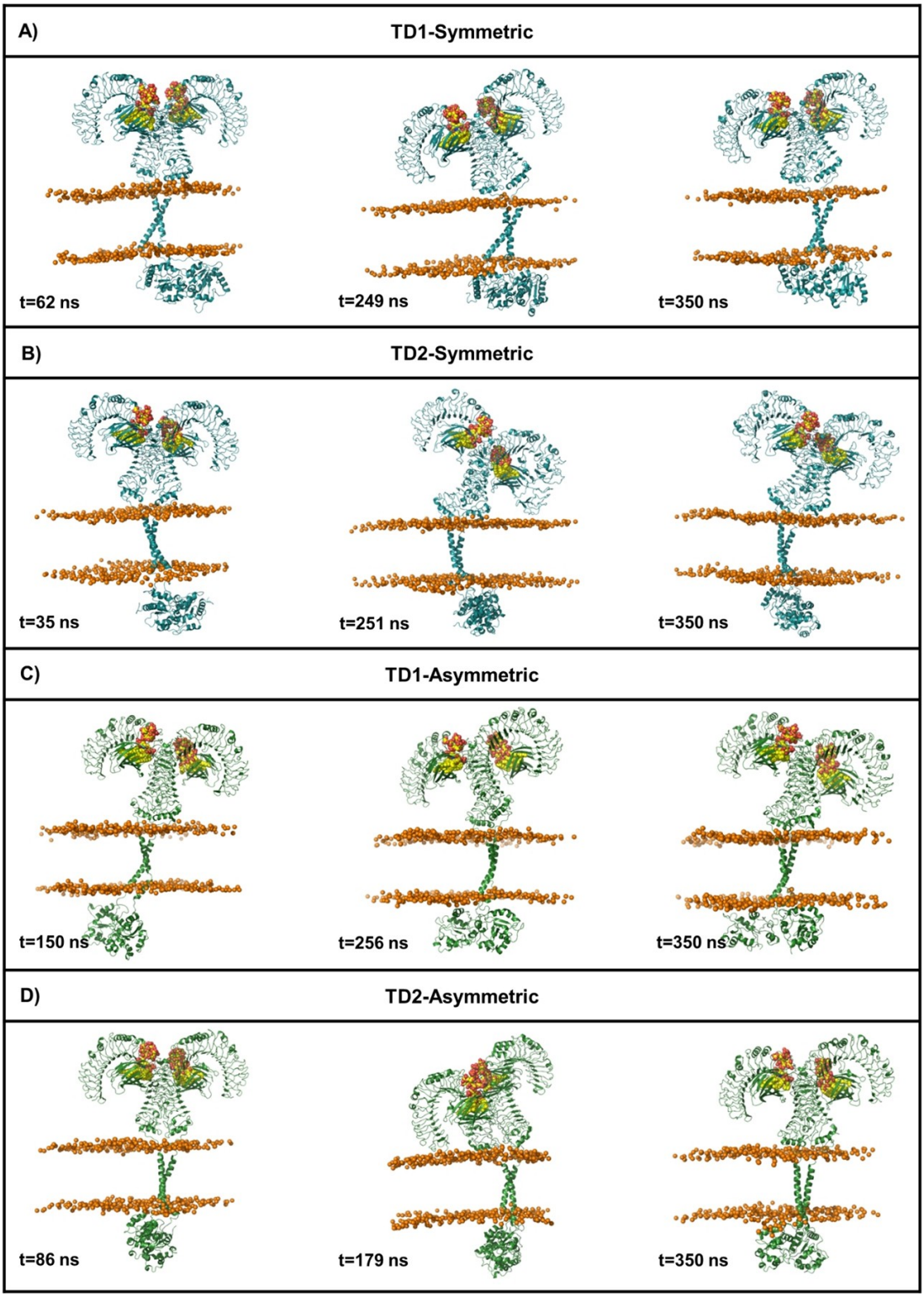


**Figure 10.** Snapshots from representative MD simulation moments show the ED bouncing movement in the A) TD1-symmetric, B) TD2-symmetric, C) TD1-asymmetric, and D) TD2-asymmetric full-length TLR4 models. TLR4 complexes are oriented facing to the viewer. TLR4 and MD-2 are depicted in blue (symmetric models) or green (asymmetric models) cartoon. $LPS_{Ec}$ are represented as yellow spheres with the phosphate groups in red. Phosphorus atoms of the phospholipid bilayer are depicted as orange spheres. For clarity, the rest of the bilayer atoms, solvent molecules and counterions are omitted.

whereas asymmetric models showed $\phi$ values in the range ~17–23°. Interestingly, $\phi$ values are in accordance with those observed in the MD simulations of the TD models in a Lo membrane (TLR4 TD section), which are $\phi$ ~20° and ~36° for

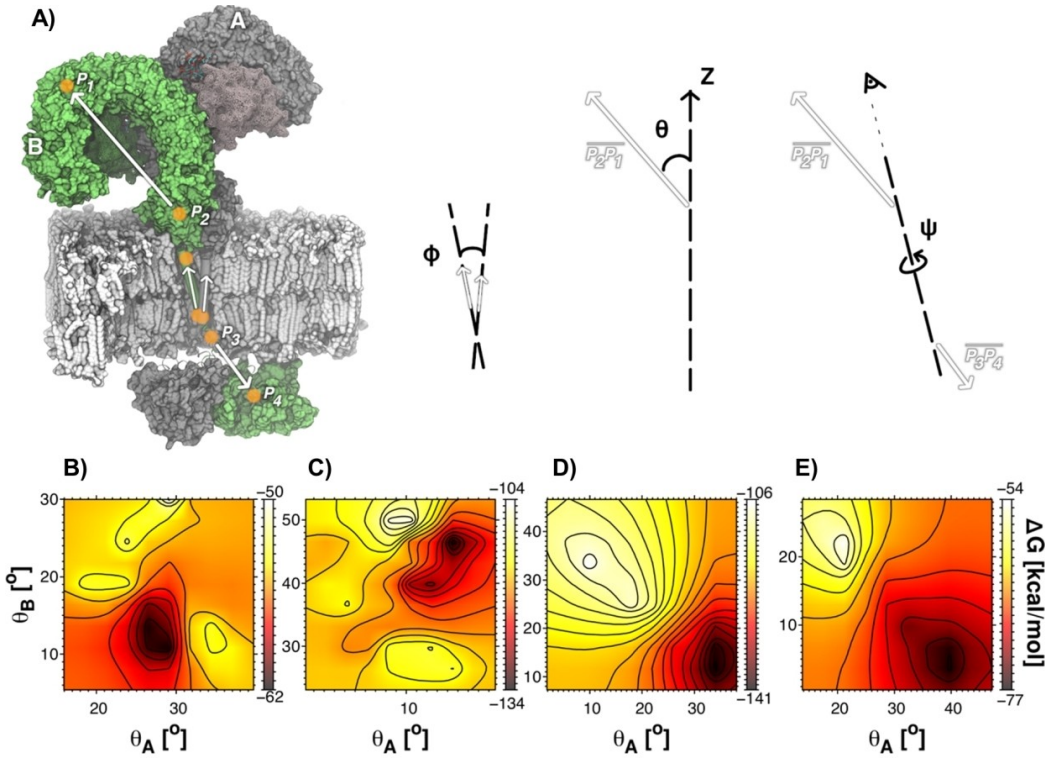


**Figure 11.** A) Definition of angles. $\theta$ is defined as the angle between the *z*-axis and the vector formed by the center of masses $P_1$ and $P_2$ in each TLR4 chain; $\psi$ is the dihedral angle formed between ED and ID ($\psi \sim 0°$: ED and ID are *anti*; $\psi \sim 180°$: ED and ID are *cis*); $\phi$ is the cross angle defined by both $\alpha$-helices at the TD. B)–E) Gibbs free energy, $\Delta G$, as a function of angles $\theta_A$ and $\theta_B$ for TD1-symmetric, TD2-symmetric, TD1-asymmetric and TD2-asymmetric, respectively. $P_1$, $P_2$, $P_3$ and $P_4$ are the centers of mass of residues 213–225, 559–573, 632–637, and 673–791 respectively.

TD1 and TD2, respectively. It suggests that isolated TLR4 TD dimers can exhibit the same crossing angles observed in a full-length model. Nevertheless, TD-TD* protein-protein interface is modified in full-length models in comparison to the one observed in isolated TD dimers (Figure S9B and S21). It seems that one TD helix is shifted toward up the membrane surface whereas the second TD* domain migrates to the membrane bottom. The TD plus the hydrophobic region (defined between residues Lys631 and Ala662) remained as $\alpha$-helix (Figure S22). The TD domains overcome the hydrophobic mismatch with the bilayer by inducing a turn in one or in both chains. This turn is observed in the HR in the TD2 models (Figure S22C and D), and it is surrounding residues Leu639 to Leu642, in the TD1 models (Figure S22A and B). The lowest energy conformations (Figure 11B–E, black spots) are observed in the TLR4 models with TD2 and symmetric ID-ID* (TD2-symmetric, Figure 11C), and with TD1 and asymmetric ID-ID* (TD1-asymmetric, Figure 11D), showing $\Delta G$ ranges of $\leq -104$ and $\leq -106$ kcal mol$^{-1}$, for the TD2-symmetric and TD1-asymmetric models, respectively. This suggests that only a given TD-TD* dimerization pattern would allow a particular ID-ID* dimerization geometry (TD1 with asymmetric ID-ID*; TD2 with symmetric ID-ID*).

### Full TLR4 dimer: Intracellular domains and membrane interactions

We also represented $\Delta G$ as a function of the dihedral angle $\psi$ for both TLR4 chains (Figures 11A and 12A–D), where $\psi$ values accounts for the relative ED–ID arrangements: *gauche* for $\psi$ ~80–90°; *cis* for $\psi$ ~40–60°; and *anti* for $\psi$ ~130–160°. An overall view indicates that the so-called symmetric models (Figure 12A and B) do not explore as many conformations given by $\psi$ values as the asymmetric full models, that is, $\psi$ ranges from 0° to 180° in the asymmetric full models for both TLR4 chains (Figure 12C and D). Favorable $\Delta G$ values are observed when an *anti* arrangement between ED and ID is obtained by a TLR4 chain, while the second chain might exhibit either a *gauche* or *cis* relative ED–ID conformation (Figure 12). The corresponding ED–ID arrangements in the most energetic favored full-length structures are shown in Figure 12E–I. In general, *anti*-conformations are favored by larger TD cross angles with $\phi$ ~32° and $\phi$ ~23° as observed in Figure 13A–D. Cross angles $\phi$ out of this range seem not to favor the *anti* and *gauche* conformations described above.

During MD simulations, the intracellular TIR domains approached to the membrane in all models, establishing mainly electrostatic interactions with the polar head groups of the membrane inner leaflet. Once the ID-ID* dimer lands to the membrane, the interactions were maintained over time for the

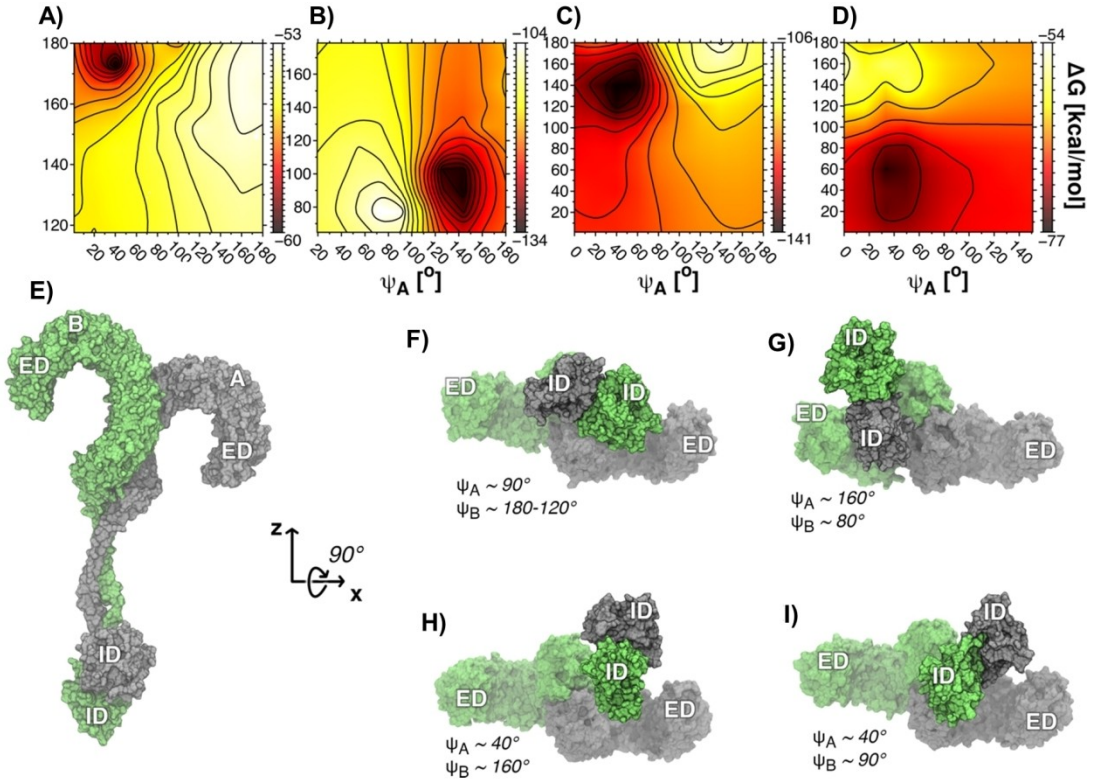


**Figure 12.** Gibbs free energy, $\Delta G$, as a function of angles $\psi_A$ and $\psi_B$ for A) TD1-symmetric, B) TD2-symmetric, C) TD1-asymmetric, and D) TD2-asymmetric models. E) Lateral-side view of TLR4-TLR4* full length (MD-2, LPS, lipids, cholesterol and water are omitted for clarity). View rotated by 90° of the TLR4-TLR4* complex for F) TD1-symmetric, G) TD2-symmetric, H) TD1-asymmetric, and I) TD2-asymmetric models.

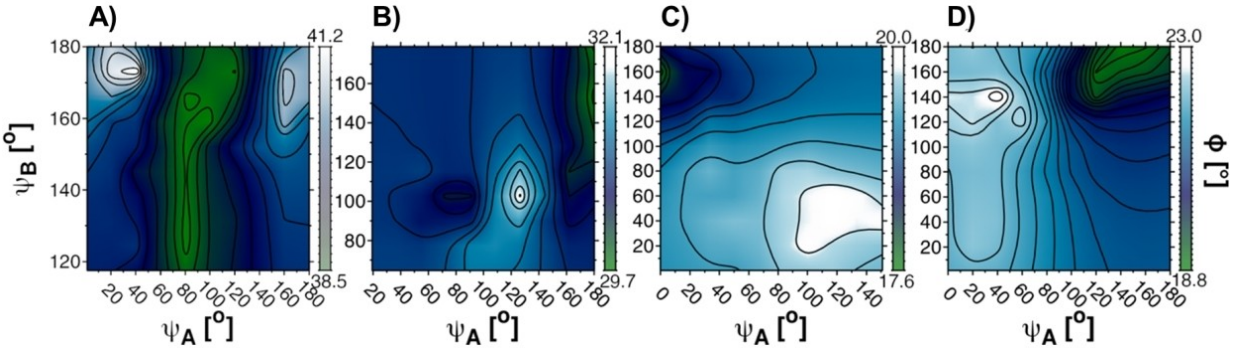


**Figure 13.** Cross angle, $\phi$ as a function of angles $\psi_A$ and $\psi_B$ for A) TD1-symmetric, B) TD2-symmetric, C) TD1-asymmetric and D) TD2-asymmetric models.

rest of the MD simulations (see snapshots in Figure 10). All models showed the same behavior for the TIR intracellular dimer (Figure 14): firstly, an ID unit approaches to the membrane and interacts with the lipids headgroups (Figure 14A and C); later, the other subunit approximates to the membrane, and finally, the two ID units interact with the bilayer (Figure 14B and D).

In the asymmetric models, the interaction occurred through residues from helixes αA and αB, and the BB loop of one monomer, and the helix αE and the AB loop of the other (Figure 14B). In the symmetric models, the ID-membrane interactions occurred through the helixes αA and AB loop of one unit and the helix αB, CD loop, and C-terminal region of the counterpart (Figure 14D). These interactions were coincident to those reported by Patra et al.[25] Note that ID-ID* dimerization interfaces were conserved in both types of full-length models, the symmetric and asymmetric ones, despite the membrane presence (TLR4 ID section for full PPI description; Figure S23).

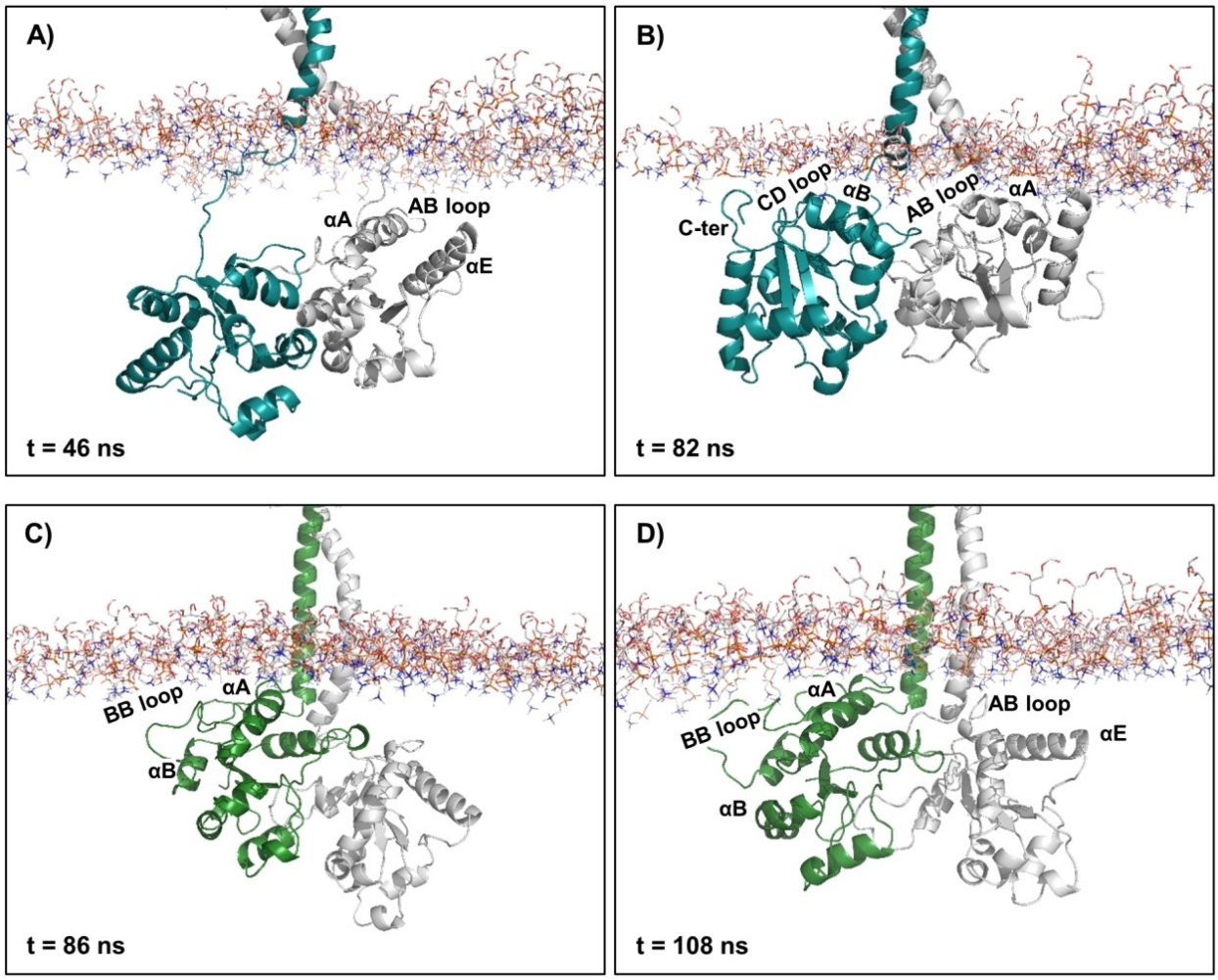


**Figure 14.** Snapshots from representative moments of MD simulations show the ID–membrane interaction in the symmetric (A, B) and asymmetric (C, D) models. TLR4 chain A is depicted in blue (symmetric model) or green (asymmetric model), and chain B as a gray cartoon. Phosphate headgroups of the membrane are depicted as gray lines. The rest of the bilayer atoms, solvent molecules, and counterions are omitted for the sake of clarity.

### Full TLR4 dimer: TLR4-MAL binding

Finally, to gain further insights into the validity of our full-length models as the active form of the TLR4 receptor, we wondered whether the lowest energy conformations of full-length models could be prone to bind downstream signaling adaptor proteins, exemplified in MAL. We superimposed our TLR4 ID/MAL docked complexes to the ID domain of the full-length models (complexes are shown in Figure S24) and observe that MAL could bind to our symmetric and asymmetric models, in an orientation geometrically compatible with MAL anchored to the membrane (Annex 5 in the Supporting Information).

Overall, our studies of the isolated TLR4 TIR dimer, and full-length TLR4, suggest that both symmetric and asymmetric ID-ID* models are suitable for MAL binding, supporting the hypothesis that both models could co-exist, and have a direct implication in the activation of distinct TLR4 pathways.

## Conclusions

Biomolecular simulations studies of the different independent domains that make up the human TLR4/MD-2 system were undertaken aiming at uncovering details of the precise mechanism of activation of the receptor. MD simulations point to a mutual stabilizing role between both extracellular TLR4/MD-2/$LPS_{Ec}$ units in the agonist (TLR4/MD-2/$LPS_{Ec}$)$_2$ dimer. Our investigations into the transmembrane domain indicate the plasticity of the hydrophobic region, depending on the membrane composition, as determinant in the dimerization of the intracellular domain, thus explaining, at the atomic and molecular levels, the necessity of TLR4 recruitment into lipid rafts during receptor activation. We also provide here several models for the transmembrane TD-TD* dimers and, altogether, these results point to a high plasticity of the TD–HR, which can adopt different conformations thus changing the mode of dimerization depending on the environment, regulated by TLR4 localization (i.e., plasma membrane or endosomal membrane).

Regarding the intracellular domain, we report two ID-ID* dimerization models, symmetric, with the αC helix and the BB loop facing at the dimerization interface, and asymmetric, in a head-to-tail fashion. Both ID-ID* models are compatible with bridging adaptor proteins binding, exemplified in stable complexes with the MAL protein. These results, together with the plasticity of the TD domain, indicate that the dimerization (and thus the activation) of TLR4 receptor is an intricate combination of membrane composition and the protein structure itself.

From the information gathered from our independent TLR4 domain studies, we finally modeled, by all-atom MD simulations, the structural assembly of plausible full-length TLR4 models embedded into a realistic plasma membrane. We supply the hypothesis, from the thermodynamic point of view, that the TD2-symmetric and TD1-asymmetric models adopt favorable conformations of the full-length receptor in lipid rafts, upon LPS binding. From the molecular point of view, both full-length TLR4 models are suitable for binding either monomeric or dimeric MAL adaptor in the plasma membrane. Thus, we suggest that both ways of dimerization could co-exist, and have a direct implication in the activation of distinct TLR4 pathways. Our comprehensive structure-energy correlations clearly suggest an *anti* ED–ID relative orientation for one of the TLR4 chains as a reasonable geometry for the $(TLR4/MD\text{-}2/LPS_{Ec})_2$ architecture accounting for the active (agonist) state. The most favorable energies are observed when the extracellular domain is tilted towards the membrane, interacting with the phospholipids head groups, pointing to a signal-transduction mechanism across the cell membrane, within lipid–TLR4 interactions. Therefore, our results concerning the effect of the membrane composition on the structure and dynamics of the TLR4 are of particular biological significance due to its role for signal transduction events. In this receptor–lipid interplay, we can speculate that the observed dynamic bouncing motion is a proper behavior for membrane receptors that can work as antennas for detecting pathogens. Our studies provide valuable insights regarding the TLR4-related innate immune pathway mechanism, opening new opportunities for advancing in the TLR4 modulation.

## Experimental Section

**Lipid membrane setup and insertion of protein systems**: All protein-membrane systems for MD simulations were generated with the membrane builder plugin from the CHARMM-GUI webserver.[60] The insertion method was selected for placing the protein into the membrane. The membranes were created with a rectangular box, and a 5 Å thick water layer on the top and bottom of the systems. The rest of the box was solvated with TIP3P water models. The systems were converted to Lipid14[61] compatible PDB format using the charmmlipid2amber.sh script. The membrane models were equilibrated for 50 ns before inserting the TD proteins. The membrane thickness can be estimated from the calculated electron density. As shown in Figure S3, a rough membrane thickness of about 46 Å for the Lo model and of 29 Å for the Ld model were observed, in agreement with data previously reported.[40,62]

**Structure optimization**: Hydrogen atoms were added to the X-ray structure of the TLR4 ED (PDB ID: 3FXI)[4] using the preprocessing tool of the Protein Preparation Wizard[63] of the Maestro package,[64] and then the structure went through a restrained minimization under the OPLS3 force field[65] with a convergence parameter to RMSD for heavy atoms kept default at 0.3 Å.

**LPS parameters derivation**: LPS structure retrieved from PDB ID: 3FXI[4] was refined at the AM1 level of theory followed by the optimization of the geometry using the density functional theory (DFT) with the hybrid functional B3LYP and the Pople basis set 6–31 + g(d,p), by means of Gaussian g09/e1.[66] Water solvation (with a dielectric constant of $\varepsilon = 78.3553$) was simulated with the Gaussian default SCRF method,[67] using the polarizable continuum model (PCM) with the integral equation formalism variant (IEFPCM).[68]

The parameters needed for MD simulations were obtained using the standard Antechamber procedure in Amber14.[69] The atomic partial charges were calculated with Gaussian g09[66] at the Hartree–Fock level (HF/6-31G* Pop = MK iop(6/33 = 2) iop(6/42 = 6)), then the partial charges were derived and formatted for AmberTools15 and Amber16 with Antechamber,[70] using the standard AMBER RESP.[71] The structure was split into residues to facilitate the parametrization process. First, the GAFF[72] atom types were assigned. Later, the atom types of the atoms constituting the saccharide ring were changed to the GLYCAM.[73] The GAFF parameters for the phosphate group were modified as shown in the Supporting Information.

**TD-TD* dimer models**: The transmembrane models (from residues Lys631 to Ala662) were predicted by submitting the TD sequence to TMDOCK and PREDDIMER webservers. The TMDOCK algorithm threads a target amino acid sequence through a fast template-driven global energy optimization procedure, whereas the PREDDIMER method is based on packing consideration, establishing the maximal complementarity of hydrophobic properties on the helix-helix interface. Sequence spanning from residue Val620 to residue Gly670 was given as input to the TMDOCK program, as the input amino acid sequence must be longer than the expected TD helix. In the case of PREDDIMER, the sequence from Lys631 to Ala662 was used as input, since the exact sequence of amino acids contained in the TD helix must be specified. The predicted models went through a restrained minimization and equilibration procedure, and then scored with the Qualitative Model Energy ANalysis (QMEAN) server, accessing the scoring function QMEANBrane.[45] QMEANBrane is a local model quality estimation method for membrane proteins that allows evaluating protein structures without knowing the target structure. QMEANBrane determines local (i.e., per residue) and global scores. The scores range from 0 to 1, with "1" being optimal.

**TD dimers cluster analysis**: Only the right-handed crossed disposition between the TD-TD* dimers was considered, since it has been reported to be predominant.[44] The left-handed crossing dimers (two models from a total of 12), and the parallel dimer (one model from a total of 12) were therefore not used for the clustering analysis. For clustering, the equilibrated right-handed crossing dimers (nine models from a total of 12) were combined into a single PDB file, using the cpptraj module of AmberTools15.[69] Clusters were constructed using the gmx cluster tool of GROMACS, using a cutoff of 4 Å.[74] The least squares fit and RMSD calculation was based on residues side chains. The clustering analysis revealed two main dimerization interfaces (interface I and II), as the 9 studied TD-TD* models were grouped into two equally populated clusters (four models were assigned to each cluster). The remaining TD dimer was not grouped in any of the two clusters.

 

**Homology modeling**: The TLR4 symmetric ID-ID* model was predicted and built within the homology modeling protocol as implemented in YASARA software.[75] TLR4 amino acid sequence spanning from residue 653 to residue 839 was given as input to the program. The homology modeling algorithm retained five templates: the TIR domains of human TLR1, TLR2 (P681h mutant), TLR2 (C713s mutant), TLR6, and TLR10, retrieved from the PDB under the accession codes 1FYV, 1FYX, 1O77, 4OM7 and 2J67, respectively. Modeling speed was set to slow, which yield best results, and rest of parameters were kept as default. To evaluate the quality of the structure of the models, we calculated the Ramachandran plots[76] using the PROCHECK webserver.[77] As showed in Table S5, percentage of 99.7 and 99.2 of the residues were in favored or allowed regions for the symmetric and asymmetric models, respectively (Table S5). These results showed that the obtained structures satisfy the Ramachandran criteria.

**Protein–protein docking**: PyDock server[78] was used to performed protein-protein docking calculations. i) For the construction of the TLR4 ID-ID* asymmetric model, a restricted docking was performed based on the mutagenesis studies reported by Bovijn et al.[50,51] The following residues were restricted in order to keep the ID-ID* protein-protein interface: Asn792, Tyr794, Glu796, Try797, Glu798 and Arg810 of one monomer and Glu698, Tyr674, Arg710, Asp711, Pro714, Arg731, Ser744, Cys747, Tyr751 and Glu752 of the counterpart. ii) For the study of the TLR4-ID/MAL PPIs, a restrained pairwise protein docking was carried out, between the two TLR4 ID-ID* models (symmetric and asymmetric) and MAL protein. Residues Ser744, Cys747, Tyr751 and Glu752 were selected in both TLR4 ID units, and Glu95, Pro149, Arg153, Lys158, Arg184, Ala185, Tyr187, Arg192 and Arg200 were restricted in the MAL protein. MAL monomer was docked towards the TLR4 ID-ID* symmetric and asymmetric dimers, and MAL-MAL dimer was docked towards the TLR4 ID-ID* asymmetric dimer. The corresponding structures of the MAL protein were extracted from the cryo-EM structure (PDB ID: 5UZB, MAL dimer corresponded to chains A and C, and MAL monomer to chain A).[6]

**Binding affinity prediction**: The PROtein binDIng enerGY prediction (PRODIGY)[79] server was used to predict the binding affinity (kcal mol$^{-1}$) of MAL protein to the TLR4 ID dimer models.

**Molecular dynamics simulations**: All-atom (AA) MD simulations were performed with Amber16.[69] The force fields ff14SB,[80] Lipid14,[61] and a combination of GAFF[72] and GLYCAM06[73] were used to described proteins, membrane phospholipids, and *E. coli* LPS, respectively. The simulation box was designed such as both the top and bottom edges are distant of at least 10 Å of any atoms. The systems were solvated with the TIP3P water molecules model. $Na^+$ and $Cl^-$ ions were added to counterbalance the charges of the systems. Two different protocols were used depending on the system. The following protocol was used for MD simulation of non-containing lipid bilayers: first, the system was minimized by 1000 steps with steepest descent algorithm followed by 7000 steps of conjugate gradient algorithm. A 100 kcal mol$^{-1}$ A$^{-2}$ harmonic potential constraint was applied on the protein. In the subsequent steps, the harmonic potential was progressively lowered (respectively to 10, 5, 2.5 and 0 kcal mol$^{-1}$ A$^{-2}$) for 600 steps with conjugate gradient algorithm each time. Next, the system was heated from 0 to 100 K applying Langevin thermostat in the canonical ensemble (NVT) under a 20 kcal mol$^{-1}$ A$^{-2}$ harmonic potential restraint on the proteins and the ligand. Finally, the system was heated up from 100 to 300 K in the isothermal–isobaric ensemble (NPT) under the same restraint condition than the previous step, followed by a simulation of 100 ps in which all harmonic restraints were removed. At this point the system was ready for the production run, which was performed using the Langevin thermostat in the NPT ensemble, at a 2 fs time step.

MD simulations including lipid bilayers and proteins were performed as follows: an energy minimization using steepest descent gradient algorithm is iterated for 5000 steps and 5000 iterations of conjugate gradient algorithm. Then, the system is heated from 0 to 100 K for 2500 steps in an NVT ensemble and positions restrains for proteins and lipids with an harmonic potential of 10 kcal mol$^{-1}$ A$^{-1}$ and applying the Langevin thermostat. Subsequently, the system is heated from 100 to 303 K for 50000 steps. Later, the system is equilibrated by 5 ns with lipids unrestrained with an anisotropic NPT ensemble and Berendsen barostat. Finally, an anisotropic NPT equilibration was run for 5 ns with all molecules unrestrained.

For all the MD simulations, the particle mesh Ewald (PME) method[81] was used to calculate long-range electrostatic interactions as implemented in AMBER16. Trajectory analysis was performed using the cpptraj module of AmberTools15.[69]

**Full-length (TLR4/MD-2/$LPS_{Ec}$)$_2$ model construction**: After the computational characterization of the individual TLR4 domains, we assembled these components into four full-length (TLR4/MD-2/$LPS_{Ec}$)$_2$ models. The agonist structure of the TLR4 ED (residues 27–627) in complex with MD-2 bounded to $LPS_{Ec}$ was retrieved from the Protein Data Bank under the accession code 3FXI.[4] The minimized and equilibrated structures of the TD1 and TD2 models in a Lo membrane environment were used as the dimeric forms of the transmembrane domain (residues 631–662). For the intracellular domain, we used the average structures from the last 30 ns of the MD simulations of the two isolated ID dimer models (symmetric and asymmetric) in water (residues 653–839). The missing residues that comprise the loops connecting the ED with the TD (residues 628–630) and the TD with the ID (residues 663–652) were added to the TD with PyMOL.[82] Then, the independent domains were manually aligned along a straight axis and placed so the distance between the C and N termini of the adjacent domains became within a bonding distance. Finally, the domains were connected together using the Maestro program.[64] The final structure was refined, as described in the structure optimization section and the inter-domain loops were further optimized using the MODLOOP server.[83]

**TLR4-TLR4* energy interaction**: Molecular mechanics generalized born surface area approach (MM-GBSA)[84] as implemented in AMBER16[69] was applied to calculated the enthalpic contribution to the protein-protein binding affinity between full-length TLR4 chains.

**MD analysis**: Trajectories were converted to GROMACS[74] suite formats by using ParmEd tools. *Contact maps:* A python script written in-house was used to determine frame a frame contacts between all atoms from residues involved in a given protein–protein interface. A contact is determined within a range of $0 \leq$ distance $\leq 0.35$ nm. *Angles $\theta$, $\phi$, $\psi$*: tcl scripts written in-house were used to determine angles with VMD software.[85] *Secondary structure analysis*: DSSP[41] program as implemented in AMBER16 was used to calculate secondary structures. *Kink angle analysis*: kink angle was analyzed using the gmx helix tool of GROMACS.[74] All of the snapshots were prepared using POV-Ray as implemented in PyMOL[86] and Tachyon as implemented in VMD software.[85]

## Acknowledgements

This work was financially supported by the Spanish Ministry for Science and Innovation (grants CTQ2014-57141-R, CTQ2017-88353-R, and PID2020-113588RB–I00; grants BES-2012-053653 for L.P.R., BES-2015-071588 for J.G.C. and PRE2018-086249 for

 

A.M.R.), and the European Commission Marie Sklodowska-Curie actions (H2020-MSCA-ITN-642157 "TOLLerant"). Gonzalo Jimenez-Oses is acknowledged for helpful discussions. S.H.J. is gratefully acknowledged for tireless support during the development of the project.

## Conflict of Interest

The authors declare no conflict of interest.

**Keywords:** membrane proteins · molecular dynamics · molecular modeling · molecular recognition · Toll-like receptors

[1] G. P. Amarante-Mendes, S. Adjemian, L. M. Branco, L. C. Zanetti, R. Weinlich, K. R. Bortoluci, *Front. Immunol.* **2018**, *9*, 2379.
[2] M. K. Vidya, V. G. Kumar, V. Sejian, M. Bagath, G. Krishnan, R. Bhatta, *Int. Rev. Immunol.* **2018**, *37*, 20–36.
[3] A. Molinaro, O. Holst, F. Di Lorenzo, M. Callaghan, A. Nurisso, G. D'Errico, A. Zamyatina, F. Peri, R. Berisio, R. Jerala, J. Jiménez-Barbero, A. Silipo, S. Martín-Santamarí, *Chem. Eur. J.* **2015**, *21*, 500–519.
[4] B. S. Park, D. H. Song, H. M. Kim, B. S. Choi, H. Lee, J. O. Lee, *Nature* **2009**, *458*, 1191–1195.
[5] T. Kawasaki, T. Kawai, *Front. Immunol.* **2014**, *5*, 461.
[6] T. Ve, P. R. Vajjhala, A. Hedger, T. Croll, F. Dimaio, S. Horsefield, X. Yu, P. Lavrencic, Z. Hassan, G. P. Morgan, A. Mansell, M. Mobli, A. O'Carroll, B. Chauvin, Y. Gambin, E. Sierecki, M. J. Landsberg, K. J. Stacey, E. H. Egelman, B. Kobe, *Nat. Struct. Mol. Biol.* **2017**, *24*, 743–751.
[7] I. Jialal, H. Kaur, S. Devaraj, *J. Clin. Endocrinol. Metab.* **2014**, *99*, 39–48.
[8] M. A. Shetab Boushehri, A. Lamprecht, *Mol. Pharm.* **2018**, *15*, 4777–4800.
[9] N. N. Kuzmich, K. V. Sivak, V. N. Chubarev, Y. B. Porozov, T. N. Savateeva-Lyubimova, F. Peri, *Vaccine* **2017**, *5*, 34.
[10] M. Smith, E. García-Martínez, M. R. Pitter, J. Fucikova, R. Spisek, L. Zitvogel, G. Kroemer, L. Galluzzi, *Oncoimmunology* **2018**, *7*, e1526250.
[11] C. H. Marzabadi, R. W. Franck, *Chem. Eur. J.* **2017**, *23*, 1728–1742.
[12] L. Zaffaroni, F. Peri, *Future Med. Chem.* **2018**, *10*, 461–476.
[13] S. M. Opal, P. F. Laterre, B. Francois, S. P. LaRosa, D. C. Angus, J. P. Mira, X. Wittebole, T. Dugernier, D. Perrotin, M. Tidswell, L. Jauregui, K. Krell, J. Pachl, T. T. C. Peckelsen, E. Cordasco, C. S. Chang, S. Oeyen, N. Aikawa, T. Maruyama, R. Schein, A. C. Kalil, M. Van Nuffelen, M. Lynn, D. P. Rossignol, J. Gogate, M. B. Roberts, J. L. Wheeler, J. L. Vincent, *JAMA J. Am. Med. Assoc.* **2013**, *309*, 1154–1162.
[14] Q. U. Ain, M. Batool, S. Choi, *Molecules* **2020**, *25*, 627.
[15] J. M. Billod, A. Lacetera, J. Guzmán-Caldentey, S. Martín-Santamaría, *Molecules* **2016**, 994.
[16] G. Van Meer, D. R. Voelker, G. W. Feigenson, *Nat. Rev. Mol. Cell Biol.* **2008**, *9*, 112–124.
[17] L. Rajendran, K. Simons, *J. Cell Sci.* **2005**, *118*, 1099–1102.
[18] J. M. Ruysschaert, C. Lonez, *Biochim. Biophys. Acta Biomembr.* **2015**, *1848*, 1860–1867.
[19] U. Ohto, K. Fukase, K. Miyake, T. Shimizu, *Proc. Natl. Acad. Sci. USA* **2012**, *109*, 7421–7426.
[20] J. Klett, J. Reeves, N. Oberhauser, L. Pérez-Regidor, S. Martín-Santamaría, *Curr. Top. Med. Chem.* **2015**, *14*, 2672–2683.
[21] K. S. Mineev, S. A. Goncharuk, M. V. Goncharuk, P. E. Volynsky, E. V. Novikova, A. S. Aresinev, *Sci. Rep.* **2017**, *7*, 1–12.
[22] D. A. Holdbrook, R. G. Huber, J. K. Marzinek, A. Stubbusch, A. Schmidtchen, P. J. Bond, *Pharmacol. Res.* **2019**, *147*, 104372.
[23] R. G. Huber, N. A. Berglund, V. Kargas, J. K. Marzinek, D. A. Holdbrook, S. Khalid, T. J. Piggot, A. Schmidtchen, P. J. Bond, *Structure* **2018**, *26*, 1151–1161.e4.
[24] J. Jumper, R. Evans, A. Pritzel, T. Green, M. Figurnov, O. Ronneberger, K. Tunyasuvunakool, R. Bates, A. Žídek, A. Potapenko, A. Bridgland, C. Meyer, S. A. A. Kohl, A. J. Ballard, A. Cowie, B. Romera-Paredes, S. Nikolov, R. Jain, J. Adler, T. Back, S. Petersen, D. Reiman, E. Clancy, M. Zielinski, M. Steinegger, M. Pacholska, T. Berghammer, S. Bodenstein, D. Silver, O. Vinyals, A. W. Senior, K. Kavukcuoglu, P. Kohli, D. Hassabis, *Nature* **2021**, *596*, 583–589.
[25] M. C. Patra, H. K. Kwon, M. Batool, S. Choi, *Front. Immunol.* **2018**, *9*, 489.
[26] E. Mobarak, L. Håversen, M. Manna, M. Rutberg, M. Levin, R. Perkins, T. Rog, I. Vattulainen, J. Borén, *Sci. Rep.* **2018**, *8*, 1–11.
[27] R. A. Corey, P. J. Stansfeld, M. S. P. Sansom, *Biochem. Soc. Trans.* **2020**, *48*, 25–37.
[28] S. J. Marrink, V. Corradi, P. C. T. Souza, H. I. Ingólfsson, D. P. Tieleman, M. S. P. Sansom, *Chem. Rev.* **2019**, *119*, 6184–6226.
[29] F. Di Lorenzo, Ł. Kubik, A. Oblak, N. I. Lorè, C. Cigana, R. Lanzetta, M. Parrilli, M. A. Hamad, A. De Soyza, A. Silipo, R. Jerala, A. Bragonzi, M. A. Valvano, S. Martín-Santamaría, A. Molinaro, *J. Biol. Chem.* **2015**, *290*, 21305–21319.
[30] C. Ciaramelli, V. Calabrese, S. E. Sestito, L. Pérez-Regidor, J. Klett, A. Oblak, R. Jerala, M. Piazza, S. Martín-Santamaría, F. Peri, *Chem. Biol. Drug Des.* **2016**, *88*, 217–229.
[31] S. E. Sestito, F. A. Facchini, I. Morbioli, J. M. Billod, S. Martín-Santamaría, A. Casnati, F. Sansone, F. Peri, *J. Med. Chem.* **2017**, *60*, 4882–4892.
[32] J. Vašl, A. Oblak, T. T. Peternelj, J. Klett, S. Martín-Santamaría, T. L. Gioannini, J. P. Weiss, R. Jerala, *J. Immunol.* **2016**, *196*, 2309–2318.
[33] T. Paramo, T. J. Piggot, C. E. Bryant, P. J. Bond, *J. Biol. Chem.* **2013**, *288*, 36215–36225.
[34] N. Resman, J. Vašl, A. Oblak, P. Pristovšek, T. L. Gioannini, J. P. Weiss, R. Jerala, *J. Biol. Chem.* **2009**, *284*, 15052–15060.
[35] The UniProt Consortium. UniProt: A Worldwide Hub of Protein Knowledge. *Nucleic Acids Res.* **2019**, *47*, 506–515.
[36] M. Treeby, J. Vašl, P. Ota, J. Friedrich, R. Jerala, *Biochem. Biophys. Res. Commun.* **2009**, *381*, 65–69.
[37] G. Panter, R. Jerala, *J. Biol. Chem.* **2011**, *286*, 23334–23344.
[38] J. M. Ruysschaert, C. Lonez, *Biochim. Biophys. Acta Biomembr.* **2015**, *1848*, 1860–1867.
[39] E. V. Bocharov, K. S. Mineev, K. V. Pavlov, S. A. Akimov, A. S. Kuznetsov, R. G. Efremov, A. S. Arseniev, *Biochim. Biophys. Acta Biomembr.* **2017**, *1859*, 561–576.
[40] R. M. Venable, F. L. H. Brown, R. W. Pastor, *Chem. Phys. Lipids* **2015**, *192*, 60–74.
[41] W. Kabsch, C. Sander, *Biopolymers* **1983**, *22*, 2577–2637.
[42] A. L. Lomize, I. D. Pogozheva, *J. Mol. Biol.* **2017**, *429*, 390–398.
[43] A. A. Polyansky, A. O. Chugunov, P. E. Volynsky, N. A. Krylov, D. E. Nolde, R. G. Efremov, *Bioinformatics* **2014**, *30*, 889–90.
[44] V. Kargas, J. K. Marzinek, D. A. Holdbrook, H. Yin, R. C. Ford, P. J. Bond, *Biochim. Biophys. Acta Biomembr.* **2017**, *1859*, 2086–2095.
[45] G. Studer, M. Biasini, T. Schwede, *Bioinformatics* **2014**, *30*, i505.
[46] J. I. Godfroy III, M. Roostan, Y. S. Moroz, I. V. Korendovych, H. Yin, *PLoS One* **2012**, *7*, e48875.
[47] S. L. Latty, J. Sakai, L. Hopkins, B. Verstak, T. Paramo, N. A. Berglund, N. J. Gay, P. J. Bond, D. Klenerman, C. E. Bryant, *eLife* **2018**, *7*, e31377.
[48] N. J. Gay, M. F. Symmons, M. Gangloff, C. E. Bryant, *Nat. Rev. Immunol.* **2014**, *14*, 546–558.
[49] V. Y. Toshchakov, H. Szmacinski, L. A. Couture, J. R. Lakowicz, S. N. Vogel, *J. Immunol.* **2011**, *186*, 4819–4827.
[50] C. Bovijn, A. S. Desmet, I. Uyttendaele, T. Van Acker, J. Tavernier, F. Peelman, *J. Biol. Chem.* **2013**, *288*, 12054–12066.
[51] C. Bovijn, P. Ulrichts, A. S. De Smet, D. Catteeuw, R. Beyaert, J. Tavernier, F. Peelman, *J. Biol. Chem.* **2012**, *287*, 4088–4098.
[52] T. Ronni, V. Agarwal, M. Haykinson, M. E. Haberland, G. Cheng, S. T. Smale, *Mol. Cell. Biol.* **2003**, *23*, 2543–2555.
[53] T. Nyman, P. Stenmark, S. Flodin, I. Johansson, M. Hammarström, P. R. Nordlund, *J. Biol. Chem.* **2008**, *283*, 11861–11865.
[54] R. Núñez-Miguel, J. Wong, J. F. Westoll, H. J. Brooks, L. A. J. O'Neill, N. J. Gay, C. E. Bryant, T. P. Monie, *PLoS One* **2007**, *2*, e788.
[55] K. Funami, M. Matsumoto, H. Oshiumi, F. Inagaki, T. Seya, *Biochem. Soc. Trans.* **2017**, *45*, 929–935.
[56] T. Ve, N. J. Gay, A. Mansell, B. Kobe, S. Kellie, *Curr. Drug Targets* **2012**, *13*, 1360–1374.
[57] A. Arkhipov, Y. Shan, R. Das, N. F. Endres, M. P. Eastwood, D. E. Wemmer, J. Kuriyan, D. E. Shaw, *Cell* **2013**, *152*, 557–569.
[58] A. C. Kalli, T. Rog, I. Vattulainen, I. D. Campbell, M. Sansom, *J. Membr. Biol.* **2017**, *250*, 337–351.
[59] E. V. Bocharov, K. S. Mineev, K. V. Pavlov, S. A. Akimov, A. S. Kuznetsov, R. G. Efremov, A. S. Arseniev, *Biochim. Biophys. Acta Biomembr.* **2017**, *1859*, 561–576.
[60] E. L. Wu, X. Cheng, S. Jo, H. Rui, K. C. Song, E. M. Dávila-Contreras, Y. Qi, J. Lee, V. Monje-Galvan, R. M. Venable, J. B. Klauda, W. Im, *J. Comput. Chem.* **2014**, *35*, 1997–2004.
[61] C. J. Dickson, B. D. Madej, Å. A. Skjevik, R. M. Betz, K. Teigen, I. R. Gould, R. C. Walker, *J. Chem. Theory Comput.* **2014**, *10*, 865–879.

 

[62] W. Rawicz, K. C. Olbrich, T. McIntosh, D. Needham, E. A. Evans, *Biophys. J.* **2000**, *79*, 328–339.
[63] G. Madhavi Sastry, M. Adzhigirey, T. Day, R. Annabhimoju, W. Sherman, *J. Comput.-Aided Mol. Des.* **2013**, *27*, 221–234.
[64] *Schrödinger Release 2020–2*: Maestro, Schrödinger, LLC, New York, NY, **2020**.
[65] E. Harder, W. Damm, J. Maple, C. Wu, M. Reboul, J. Y. Xiang, L. Wang, D. Lupyan, M. K. Dahlgren, J. L. Knight, J. W. Kaus, D. S. Cerutti, G. Krilov, W. L. Jorgensen, R. Abel, R. A. Friesner, *J. Chem. Theory Comput.* **2016**, *12*, 281–296.
[66] M. J. Frisch, G. W. Trucks, H. B. Schlegel, G. E. Scuseria, M. A. Robb, J. R. Cheeseman, G. Scalmani, V. Barone, B. Mennucci, G. A. Petersson, H. Nakatsuji, M. Caricato, X. Li, H. P. Hratchian, A. F. Izmaylov, J. Bloino, G. Zheng, J. L. Sonnenberg, M. Hada, M. Ehara, K. Toyota, R. Fukuda, J. Hasegawa, M. Ishida, T. Nakajima, Y. Honda, O. Kitao, H. Nakai, T. Vreven, J. A. Montgomery, Jr., J. E. Peralta, F. Ogliaro, M. Bearpark, J. J. Heyd, E. Brothers, K. N. Kudin, V. N. Staroverov, R. Kobayashi, J. Normand, K. Raghavachari, A. Rendell, J. C. Burant, S. S. Iyengar, J. Tomasi, M. Cossi, N. Rega, J. M. Millam, M. Klene, J. E. Knox, J. B. Cross, V. Bakken, C. Adamo, J. Jaramillo, R. Gomperts, R. E. Stratmann, O. Yazyev, A. J. Austin, R. Cammi, C. Pomelli, J. W. Ochterski, R. L. Martin, K. Morokuma, V. G. Zakrzewski, G. A. Voth, P. Salvador, J. J. Dannenberg, S. Dapprich, A. D. Daniels, Ö. Farkas, J. B. Foresman, J. V. Ortiz, J. Cioslowski, and D. J. Fox, *Gaussian 09*, Revision A.02, Gaussian, Inc., Wallingford CT.
[67] T. Ve, S. J. Williams, B. Kobe, *Apoptosis* **2015**, *20*, 250–261.
[68] J. Tomasi, B. Mennucci, R. Cammi, *Chem. Rev.* **2005**, *105*, 2999–3093.
[69] D. A. Case, I. Y. Ben-Shalom, S. R. Brozell, D. S. Cerutti, T. E. Cheatham III, V. W. D. Cruzeiro, T. A. Darden, R. E. Duke, D. Ghoreishi, M. K. Gilson, H. Gohlke, A. W. Goetz, D. Greene, R Harris, N. Homeyer, S. Izadi, A. Kovalenko, T. Kurtzman, T. S. Lee, S. LeGrand, P. Li, C. Lin, J. Liu, T. Luchko, R. Luo, D. J. Mermelstein, K. M. Merz, Y. Miao, G. Monard, C. Nguyen, H. Nguyen, I. Omelyan, A. Onufriev, F. Pan, R. Qi, D. R. Roe, A. Roitberg, C. Sagui, S. Schott-Verdugo, J. Shen, C. L. Simmerling, J. Smith, R. Salomon-Ferrer, J. Swails, R. C. Walker, J. Wang, H. Wei, R. M. Wolf, X. Wu, L. Xiao, D. M. York, P. A. Kollman, *AMBER 2016*, University of California, San Francisco, **2016**.
[70] J. Wang, W. Wang, P. A. Kollman, D. A. Case, *J. Mol. Graphics Modell.* **2006**, *25*, 247–260.
[71] C. I. Bayly, P. Cieplak, W. D. Cornell, P. A. Kollman, *J. Phys. Chem.* **1993**, *97*, 10269–10280.
[72] J. Wang, R. M. Wolf, J. W. Caldwell, P. A. Kollman, D. A. Case, *J. Comput. Chem.* **2004**, *25*, 1157–1174.
[73] K. N. Kirschner, A. B. Yongye, S. M. Tschampel, J. González-Outeiriño, C. R. Daniels, B. L. Foley, R. J. Woods, *J. Comput. Chem.* **2008**, *29*, 622–655.
[74] M. J. Abraham, T. Murtola, R. Schulz, S. Páll, J. C. Smith, B. Hess, E. Lindah, *SoftwareX* **2015**, *1–2*, 19–25.
[75] H. Land, M. S. Humble, *Methods Mol. Biol.* **2018**, 1685, 43–67.
[76] S. A. Hollingsworth, P. A. Karplus, *Biomol. Concepts* **2010**, *1*, 271–283.
[77] R. A. Laskowski, M. W. MacArthur, D. S. Moss, J. M. Thornton, *J. Appl. Crystallogr.* **1993**, *26*, 283–291.
[78] T. M. K. Cheng, T. L. Blundell, J. Fernandez-Recio, *Proteins Struct. Funct. Genet.* **2007**, *68*, 503–515.
[79] L. C. Xue, J. P. Rodrigues, P. L. Kastritis, A. M. Bonvin, A. Vangone, *Bioinformatics* **2016**, *32*, 3676–3678.
[80] J. A. Maier, C. Martinez, K. Kasavajhala, L. Wickstrom, K. E. Hauser, C. Simmerling, *J. Chem. Theory Comput.* **2015**, *11*, 3696–3713.
[81] U. Essmann, L. Perera, M. L. Berkowitz, T. Darden, H. Lee, L. G. Pedersen, *J. Chem. Phys.* **1995**, *103*, 8577–8593.
[82] *The PyMOL Molecular Graphics System*, Version 2.0 Schrödinger, LLC.
[83] A. Fiser, A. Sali, *Bioinforma. Appl.* **2003**, *19*, 2500–2501.
[84] W. Clark Still, A. Tempczyk, R. C. Hawley, T. Hendrickson, *J. Am. Chem. Soc.* **1990**, *112*, 6127–6129.
[85] W. Humphrey, A. Dalke, K. Schulten, *J. Mol. Graphics* **1996**, *14*, 33–38.
[86] POVRAY 3.6. Persistence of Vision Pty. Ltd.: Williamstown, Victoria, Australia, 2004. Available online: http://www.povray.org/download/ (accessed on 14.09.2021).

Manuscript received: August 16, 2021
Accepted manuscript online: September 26, 2021
Version of record online: October 12, 2021

 